Decay of Persistent Current in a Two-Dimensional Superfluid

Rob G. McDonald

September 2013

A dissertation submitted in partial fulfilment for
the degree of Bachelor of Science with Honours in Physics

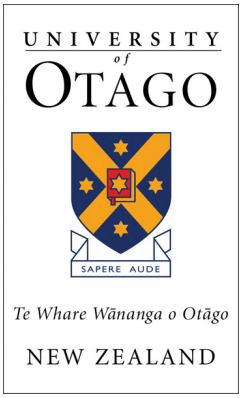

Abstract

Persistent currents, which consist of dissipationless, time-invariant, superfluid flow in periodic traps, are an active area of research. Notable aspects being investigated include the formation, stability, and decay of these currents, especially in the context of Bose-Einstein condensates.

We present a study of persistent current decay in quasi-two-dimensional Bose-Einstein condensates using a phenomenologically damped hybrid Lagrangian variational model, a modification of the Gross-Pitaevskii model. Decay is stimulated with the introduction of either an object or aperture, simulating the presence of a stationary laser beam or beams formerly in rotational equilibrium with the condensate.

We investigate the hybrid Lagrangian variational method of modelling Bose-Einstein condensates. We then analyse the decay of vortex dipoles in a persistent current. Finally, we investigate persistent current decay by performing a sequence of simulations over a range of obstruction and current parameters. This is done to probe the nature of current decay induced by the presence of an obstacle or aperture.

We find that the hybrid Lagrangian variational method provides a description consistent with the Thomas-Fermi approximation. Simulations of obstacle and aperture induced current decays show that decay depends on both obstacle or aperture size and initial current values. Further investigations show that the polarisation or annihilation of dipoles play an important role in the current decay.

Acknowledgements

soon...

Contents

Chapter 1

Introduction

Since the discovery of superfluid helium-4 in 1937, the phenomena of superfluidity has been of much interest in low-temperature physics. One of the main reasons for this interest is that superfluidity is one of only a few macroscopic quantum mechanical phenomena. Superfluidity is closely related to Bose-Einstein condensation, although they are not the same phenomena; not all superfluids are Bose-Einstein condensates, and vice versa. The definition of superfluidity is fluid flow with zero viscosity, a property which can lead to the existent of persistent currents, or flow without dissipation.

Important analysis of superfluid helium was published in 1941 in an influential paper by L. D. Landau. Among other things, Landau's paper considered the minimum velocity at which a superfluid must flow through a capillary to induce excitations, by considering the Galilean transformations of energy and momentum. In 1972, Feynman considered the minimum velocity at which a superfluid must flow out of a channel into a reservoir for excitations to occur, where the excitations are considered to be vortex-anti-vortex pairs. These two critical velocities are closely related to the onset of dissipation in superfluid flow, which is an active area of research. How the two critical velocities are related to each other is a question that has yet to be solved.

Superfluid helium was the medium in which quantum turbulence was first observed, consisting of entangled quantum vortices. However, it is not ideal to study quantum turbulence in superfluid helium; the high inter-particle interactions present cause problems in constructing a theoretical framework with which to model the dynamics. Thus, experiments in this area are now often performed using superfluid Bose-Einstein condensates, due to their high level of controllability. Quantum turbulence itself is of great interest as the quantisation of rotation of quantum vortices causes quantum turbulence to be much simpler than classical turbulence [1]. It is then hoped that the study of quantum turbulence may lead to improvements in theories of classical turbulence.

Bose-Einstein condensates can be relatively easily trapped in such a way that they are quasi-two-dimensional, having excitations in one dimension frozen out. This then provides a medium through which to study two-dimensional turbulence. Many important fluid systems can be modelled with a two-dimensional description if the scale of horizontal flows are much larger than the scale of vertical flows. Apart from requiring less computational resources

to model, a two-dimensional description also results in different physical behaviour to three dimensions.

In this work we focus on the decay of persistent current in superfluid Bose-Einstein condensates, which we simulate using a hybrid Lagrangian variational model as described by Edwards *et al.* This model allows consideration of systems with two-dimensional vortex motion, but within a regime with significant three-dimensional aspects. We stimulate the decay by creating a persistent current in a toroidally trapped condensate containing a Gaussian obstacle or aperture, which describes the condensate being stirred with the obstacle or aperture to an equilibrium state before abruptly halting the motion of the stirrer.

Chapter 2

Background

Here we discuss the background relevant to this work. We begin with a brief discussion of classical fluids, including a brief description of two-dimensional fluids. We then move on to quantum fluids, where investigations were first performed with liquid helium, and have now progressed to include Bose-Einstein condensates. We discuss the Gross-Pitaevskii equation which can be used to describe a condensed Bose gas, as well as a modification to the two-dimensional Gross-Pitaevskii equation. We then introduce the concept of quantum fluids, before discussing some key phenomena present in superfluids.

2.1 Classical Fluids

The motions of fluids are of much theoretical and practical interest in the fields of physics and engineering. In particular, turbulence is a very old unsolved problem in classical physics. Fluid flows are present in all corners of the universe, from the flow of blood through veins and arteries, to inter-galactic plasmas. Because of this, understanding fluid flows is of great importance; in particular much time is spent in engineering trying to minimise or maximise turbulence. Meteorologists and oceanographers would benefit greatly from a complete theory of fluid flow and turbulence to help predict weather and ocean currents. These are just some examples of where understanding fluid flow is of importance.

2.1.1 Fluid Dynamics

The motion of a classical viscous fluid is governed by the Navier-Stokes equation

$$\frac{\partial \mathbf{v}}{\partial t} + (\mathbf{v} \cdot \nabla)\,\mathbf{v} = -\frac{1}{\rho}\nabla p + \nu \nabla^2 \mathbf{v} + \mathbf{f}, \tag{2.1}$$

where $\mathbf{v}$ is the fluid velocity, ρ is the fluid density, p is the pressure, ν is the kinematic viscosity, and $\mathbf{f}$ is any external forcing on the fluid. The kinematic viscosity is the molecular viscosity μ divided by the density. The Navier-Stokes equation is obtained by applying conservation of mass and momentum to an ideal fluid particle in the reference frame of the fluid particle [2]. The frame choice brings out the term $(\mathbf{v} \cdot \nabla)\,\mathbf{v}$, called the *inertial term*. This term causes non-linearity in the equation, and renders it analytically unsolvable for all but the most simple systems. The Navier-Stokes equation is often accompanied by the condition for incompressible flow

$$\nabla \cdot \mathbf{v} = 0. \tag{2.2}$$

Using the definition of vorticity $\boldsymbol{\omega} = \nabla \times \mathbf{v}$, the Navier-Stokes equation takes the form

$$\frac{\partial \boldsymbol{\omega}}{\partial t} - (\boldsymbol{\omega} \cdot \nabla)\,\mathbf{v} + (\mathbf{v} \cdot \nabla)\,\boldsymbol{\omega} = \nu \nabla^2 \boldsymbol{\omega} + \mathbf{g} \tag{2.3}$$

where $\mathbf{g} = \nabla \times \mathbf{f}$. This form is often useful when considering flows containing rotation.

In some situations, it may be appropriate to neglect the viscosity of a fluid. This approximation used in conjunction with equation (2.1) leads to the Euler equation for ideal fluid flow

$$\frac{\partial \mathbf{v}}{\partial t} + (\mathbf{v} \cdot \nabla)\,\mathbf{v} = -\frac{1}{\rho}\nabla p + \mathbf{f}. \tag{2.4}$$

This idealisation reduces the Navier-Stokes equation to a first order partial differential equation, however the non-linearity ensures that computational methods are generally required to find solutions. Due to the large range of length scales involved in turbulent fluid flow, the computations are generally quite intensive, requiring a fine numerical grid and small time steps.

2.1.2 Reynolds Number

The Reynolds number is a dimensionless value the magnitude of which is used to distinguish between regimes of laminar and turbulent flow in a system. In general, a large Reynolds number indicates a turbulent flow, while a low Reynolds number indicates a laminar flow. The Reynolds number is defined by

$$Re = \frac{UL}{\nu} \tag{2.5}$$

where U is a characteristic velocity of the flow, and L is a length scale describing the flow. For example, for flow past an obstacle, U is the incident flow velocity while L is the width of the obstacle. The physical meaning of the Reynolds number is a measure of the ratio of inertial and viscous forces in the fluid. The value of the Reynolds number required for turbulent flow to occur is generally dependent on the nature of the system. The limit $Re \to \infty$, is often referred to as fully developed turbulent flow or, due to the definition of the Reynolds number, the zero-viscosity limit.

2.1.3 Two-Dimensional Fluids

Though true two-dimensional systems may be non-existent, the approximation can be valid in circumstances where spatial extent of confinement of one dimension of the fluid is much smaller than that of the other two. For example, atmospheres and oceans can be modelled as two-dimensional systems, depending on the particular aspect of the system being analysed. A two-dimensional consideration is beneficial as it is much less computationally intensive to solve. Furthermore two-dimensional systems can exhibit behaviour differing from three-dimensional systems making them interesting to study in their own right.

In two-dimensional fluids, the vorticity becomes a scalar $\omega = \omega(\mathbf{x}, t)$, and the vorticity form of the Navier-Stokes equation becomes

$$\frac{\partial \omega}{\partial t} + \mathbf{v} \cdot \nabla \omega = \nu \nabla^2 \omega + g. \tag{2.6}$$

This form is particularly useful as the velocity components are not independent (from the incompressibility condition), and thus the equation is for a scalar. Absent from the two-dimensional form is the *vortex stretching term* $-(\boldsymbol{\omega}\cdot\nabla)\,\mathbf{v}$; this is an important difference between two and three-dimensional fluids.

In the absence of forcing and viscosity, the Navier-Stokes equation becomes

$$\frac{\partial\omega}{\partial t}+\mathbf{v}\cdot\nabla\omega=0, \tag{2.7}$$

which we note is the definition of the material derivative of the vorticity, so

$$\frac{D\omega}{Dt}=0. \tag{2.8}$$

The material derivative in this case describes the rate of change of vorticity in a small volume moving with the fluid flow. The physical meaning of this equation is that the vorticity of a fluid particle is conserved. Consequently, for any continuous functions $f(\omega)$, integrals of the form

$$C_f=\int f(\omega)d^2\mathbf{x} \tag{2.9}$$

are also conserved. A notable example is the *winding*

$$\Gamma=\frac{1}{A}\int\omega d^2\mathbf{x}, \tag{2.10}$$

where A is the area of the system. The winding is an important parameter of the system that will be discussed later in this chapter.

2.2 Quantum Fluids

Even with the approximations suggested, the Navier-Stokes equation is still analytically unsolvable for the vast majority of systems, even in the absence of turbulent flow. With turbulent flow included, the problem is extremely complicated, as there are many properties of turbulence that are not fully understood. Thus much interest has turned to turbulence and fluid flow in quantum fluids [3]. With respect to turbulence, one of the main motivations is to hopefully gain some insight into classical turbulence from quantum turbulence, as it is simpler due to the quantized nature of quantum vortices. The properties of quantum fluids also result in intriguing phenomena, such as the existence of persistence currents [4], Rollin films [5], and the fountain effect [6].

2.2.1 Bose-Einstein Condensation

Bose-Einstein condensation was predicted by Einstein in 1925, prior to the development of modern quantum mechanics. Einstein predicted that below some critical temperature, an ideal Bose gas would undergo a transition to a phase where macroscopic occupation of the lowest energy state is statistically favourable. For a Bose gas trapped in a three-dimensional box the critical temperature is given by

$$T_c=\frac{2\pi\hbar^2}{mk_B}\left(\frac{\rho}{\zeta(3/2)}\right)^{2/3} \tag{2.11}$$

where ζ is the Riemann zeta function, m is the mass of the individual gas particles, and ρ is the particle density. This phenomenon allows the particles in the condensate to be described by a single wavefunction at temperatures much less than T_c.

With the development of laser cooling, Bose-Einstein condensation was able to be fully realised in 1995 using atoms of ^{87}Rb [7]. Since then there has been much research into the properties of Bose-Einstein condensates [8].

2.2.2 The Gross-Pitaevskii Equation

The second quantised Hamiltonian describing the time evolution of a Bose field is

$$\begin{aligned}\hat{H} = &\int d^3\mathbf{x}\hat{\Psi}^\dagger(\mathbf{x},t)\hat{H}_o\hat{\Psi}(\mathbf{x},t) \\ &+ \frac{1}{2}\int d^3\mathbf{x}\int d^3\mathbf{x}'\hat{\Psi}^\dagger(\mathbf{x},t)\hat{\Psi}^\dagger(\mathbf{x}',t)V_{\text{int}}(\mathbf{x},\mathbf{x}')\hat{\Psi}(\mathbf{x}',t)\hat{\Psi}(\mathbf{x},t)\end{aligned} \tag{2.12}$$

where $\hat{\Psi}(\mathbf{x},t)$ is the Bose field operator, $V_{\text{int}}(\mathbf{x},\mathbf{x}')$ is the potential of the inter-particle interactions, and $\hat{H}_o = -\frac{\hbar^2\nabla^2}{2m} + V(\mathbf{x})$ is the single particle Hamiltonian, where $V(\mathbf{x})$ is the external potential. The Bose commutation relations are

$$[\hat{\Psi}(\mathbf{x},t),\hat{\Psi}^\dagger(\mathbf{x}',t)] = \delta(\mathbf{x}-\mathbf{x}'), \quad [\hat{\Psi}(\mathbf{x},t),\hat{\Psi}(\mathbf{x}',t)] = [\hat{\Psi}^\dagger(\mathbf{x},t),\hat{\Psi}^\dagger(\mathbf{x}',t)] = 0. \tag{2.13}$$

It is then assumed that the inter-particle potential can be written in the form

$$V_{\text{int}}(\mathbf{x},\mathbf{x}') = g\delta(\mathbf{x}-\mathbf{x}'), \tag{2.14}$$

where g is the inter-particle interaction strength, related to the s-wave scattering length of the particles a by

$$g = \frac{4\pi\hbar^2 a}{m}. \tag{2.15}$$

This is known as the cold-collision approximation, and it amounts to assuming that the collisions between particles are elastic. The second quantised Hamiltonian then becomes

$$\hat{H} = \int d^3\mathbf{x}\hat{\Psi}^\dagger(\mathbf{x},t)\hat{H}_o\hat{\Psi}(\mathbf{x},t) + \frac{g}{2}\int d^3\mathbf{x}\hat{\Psi}^\dagger(\mathbf{x},t)\hat{\Psi}^\dagger(\mathbf{x},t)\hat{\Psi}(\mathbf{x},t)\hat{\Psi}(\mathbf{x},t). \tag{2.16}$$

Using the Bose commutation relations the Heisenberg equation of motion is then

$$i\hbar\frac{\partial\hat{\Psi}(\mathbf{x},t)}{\partial t} = \left[-\frac{\hbar^2\nabla^2}{2m} + V_{\text{trap}}(\mathbf{x}) + g\hat{\Psi}^\dagger(\mathbf{x},t)\hat{\Psi}(\mathbf{x},t)\right]\hat{\Psi}(\mathbf{x},t). \tag{2.17}$$

For $T \ll T_c$ and $N \gg 1$, the mean-field approximation can be applied, replacing the field operators $\hat{\Psi}(\mathbf{x},t)$ with their expectation values $\langle\Psi(\mathbf{x},t)\rangle = \Psi(\mathbf{x},t)$, which are classical fields. The result is the time-dependent Gross-Pitaevskii equation (GPE)

$$i\hbar\frac{\partial\Psi(\mathbf{x},t)}{\partial t} = \left[-\frac{\hbar^2}{2m}\nabla^2 + V_{\text{trap}}(\mathbf{x}) + g|\Psi(\mathbf{x},t)|^2\right]\Psi(\mathbf{x},t), \tag{2.18}$$

which describes the time evolution of a Bose-Einstein condensate in the mean-field and cold-collision approximations. This approach has been very successful, giving accurate descriptions

of experiments in the regime described by these approximations. The solution of the Gross-Pitaevskii equation is normalised such that

$$\int d^3\mathbf{x}|\Psi(\mathbf{x},t)|^2 = N, \tag{2.19}$$

where N is the number of particles in the condensate.

The GPE takes the form of a non-linear Schrödinger equation, and does not take into consideration condensate depletion due to thermal effects and interactions. This is a valid approximation provided that $N \gg 1$, the temperature of the condensate is well below T_c, so most of the atoms are in the ground state, and the scattering length is much less than the inter-atomic spacing. In general, the nonlinearity resulting from the inter-particle interactions renders this equation analytically unsolvable, so computational methods must be applied. However some notable analytical solutions do exist, such as solitons in one-dimensional systems.

Quasi-2D Condensates

For trapping of the form

$$V_{\text{trap}}(\mathbf{x}) = \frac{m\omega_r^2 r^2}{2} + \frac{m\omega_z^2 z^2}{2}, \tag{2.20}$$

we may define the *anisotropy* of the system as

$$\lambda = \omega_z/\omega_r \tag{2.21}$$

where ω_r is the harmonic trapping frequency in the x-y plane, ω_z is the harmonic trapping frequency in the z dimension, and $r^2 = x^2 + y^2$ is the radial distance from the z-axis.

For a system where the confinement in one dimension is much stronger than in the other two, that is, with a high anisotropy, it is possible to treat the system as being quasi two-dimensional. The high trapping suppresses excitations in the tightly confined dimension, forcing this component of the wavefunction to tend to a harmonic ground state. In this situation, it is appropriate to separate the wavefunction into a time-dependent radial component and a stationary axial component

$$\Psi(x,y,x,t) = \Phi(x,y,t)\chi(z) \tag{2.22}$$

where $\chi(z)$ is the ground state of the harmonic oscillator in the z dimension. The time evolution is then governed by by the two-dimensional time-dependent GPE

$$i\hbar\frac{\partial\Phi(x,y,t)}{\partial t} = \left[-\frac{\hbar^2}{2m}\left(\frac{\partial^2}{\partial x^2} + \frac{\partial^2}{\partial y^2}\right) + V_{||}(x,y) + g_{2D}|\Phi(x,y,t)|^2\right]\Phi(x,y,t). \tag{2.23}$$

where $\Phi(x,y,t)$ is the two-dimensional wavefunction, $V_{||}(x,y)$ is the trapping potential in the x-y plane, and g_{2D} is the two-dimensional interaction parameter, which is given by

$$g_{2D} = \frac{g}{\sqrt{2\pi}l_z} \tag{2.24}$$

where $l_z = \sqrt{\hbar/m\omega_z}$ is the harmonic oscillator length in the z direction.

For a condensate to be considered two-dimensional, the harmonic oscillator energy in the z direction must be much greater than any other characteristic energies of the system

$$\hbar\omega_z \gg \hbar\omega_x, \hbar\omega_y, \mu, k_B T. \tag{2.25}$$

In particular this requires a high level of anisotropy, and tends to restrict the system size and thus also the condensate particle number; introducing more particles into a quasi-two-dimensional condensate will eventually violate equation (2.25) and cause the condensate to become more three-dimensional.

The Hybrid Lagrangian Variational Model

Systems created in experiments have often not fulfilled the requirements for being treated as two-dimensional; motion is still possible in the tightly confined dimension. However, many of the observed dynamics have been characteristic of two-dimensional systems [9]. This suggests that, while a completely two-dimensional treatment may be making too much of an approximation, a full three-dimensional treatment may not be necessary. We thus require a modification to the Gross-Pitaevskii theory which allows some motion in a tightly confined dimension, but still contains two-dimensional dynamics. The hybrid Lagrangian variational method [10] (see section (4.1)) satisfies this by allowing the thickness of the condensate to vary in time. It also requires less computational resources to solve than the three-dimensional time-dependent GPE. The result of this method is that we now have a time-dependent effective two-dimensional interaction strength

$$g_e(t) = \frac{g}{\sqrt{2\pi} w(t)} \tag{2.26}$$

replacing g_{2D} in equation (2.23), where $w(t)$ is the Gaussian thickness of the condensate in the z dimension. The Gaussian thickness $w(t)$ evolves according to

$$\ddot{w}(t) + \omega_z^2 w(t) = \frac{\hbar^2}{m^2}\frac{1}{w^3(t)} + \frac{g_e(t)}{m w(t) N} U_{||}(x, y, t) \tag{2.27}$$

which is coupled to the Gross-Pitaevskii equation via the factor

$$U_{||}(x, y, t) = \int d^2\mathbf{x} |\Phi(x, y, t)|^4. \tag{2.28}$$

Looking for solutions to the two-dimensional Gross-Pitaevskii equation of the form $\Phi(x, y, t) = \phi(x, y) e^{i\mu t/\hbar}$, where μ is the chemical potential of the condensate, gives us the time-dependent Gross-Pitaevskii equation

$$\mu\phi(x, y) = \left[-\frac{\hbar^2}{2m}\left(\frac{\partial^2}{\partial x^2} + \frac{\partial^2}{\partial y^2} \right) + V_{||}(x, y) + g_{2D}|\phi(x, y)|^2 \right] \phi(x, y) \tag{2.29}$$

where

$$g_o = \frac{g}{\sqrt{2\pi} w_o}, \tag{2.30}$$

and w_o is the solution of the time-independent stationary form of equation (2.27)

$$\omega_z^2 w_o - \frac{\hbar^2}{m^2}\frac{1}{w_o^3} - \frac{g_o}{m w_o N} U_{||} = 0. \tag{2.31}$$

Equations (2.27) and (2.23), with g_{2D} replaced by $g_e(t)$, may be referred to as the hybrid Lagrangian variational method (HLVM) equations of motion The main advantage of HLVM is that the restrictions of equation (2.25) are relaxed,

$$\hbar\omega_z \gtrsim \hbar\omega_x, \hbar\omega_y, \mu, k_B T. \tag{2.32}$$

so we can use a two dimensional treatment when the oscillator energy in the strongly confined dimension is only approximately greater than the other characteristic energies. This allows us to use a two-dimensional treatment with systems where vortex motion may be two-dimensional [11], while the BEC is three-dimensional. In particular Edwards et al [10] showed that systems with anisotropies as low as $\lambda = 3$ modelled by the HLVM equations of motion give dynamics consistent with those given by the 3D GPE.

2.2.3 Hydrodynamic Equations

We can recast the Gross-Pitaevskii equation into a hydrodynamic form using the Madelung transformation [12]

$$\Phi(x, y, t) = \sqrt{\rho(x, y, t)} e^{i\theta(x,y,t)}, \tag{2.33}$$

where $\rho(x, y, t) = \sqrt{|\Phi(x, y, t)|^2}$ is the density of the condensate and $\theta(x, y, t)$ is the phase of the condensate wavefunction. Equating the real parts results in a continuity equation

$$\frac{\partial \rho}{\partial t} + \nabla \cdot (\rho \mathbf{v}) = 0 \tag{2.34}$$

while equating the imaginary parts results in a quantum Euler equation

$$\frac{\partial \mathbf{v}}{\partial t} + (\mathbf{v} \cdot \nabla)\, \mathbf{v} = \frac{1}{m} \nabla \left(\frac{\hbar^2}{2m} \frac{\nabla^2 \sqrt{\rho}}{\sqrt{\rho}} \right) - \frac{g_e(t)}{m} \nabla \rho - \frac{1}{m} \nabla V_{||}. \tag{2.35}$$

The first term on the right-hand side is the *quantum pressure* term, which can generally be neglected except where density gradients are high and density is low, such as in the core of a vortex. Comparing these to the classical hydrodynamic equations (2.1) and (2.2) shows us that the Gross-Pitaevskii model can be thought of as a quantum fluid model, similar to the model for a classical fluid with no viscosity. However the equations show that Bose-Einstein condensates are compressible, unlike many of the fluids considered in classical fluid dynamics.

2.2.4 Quantum Vortices

In a superfluid, vortices are topological stable structures that carry angular momentum. Because the wavefunction of the condensate must be singularly valued, the phase of the condensate is well-defined. Again utilising the Madelung transformation, we can then define the superfluid velocity as

$$\mathbf{v} = \frac{\hbar}{m} \nabla \theta. \tag{2.36}$$

The phase of the condensate is only defined up to multiples of 2π, since only relative phases have any physical meaning. Thus the line integral of the phase gradient around any point in the condensate must be an integer multiple of 2π. The winding around a contour in the condensate is then given by

$$\Gamma = \oint \mathbf{v} \cdot d\mathbf{l} = \frac{\hbar}{m} \oint \nabla \theta \cdot d\mathbf{l} = \frac{\hbar}{m} \Delta\theta = \frac{\hbar}{m} 2\pi n \tag{2.37}$$

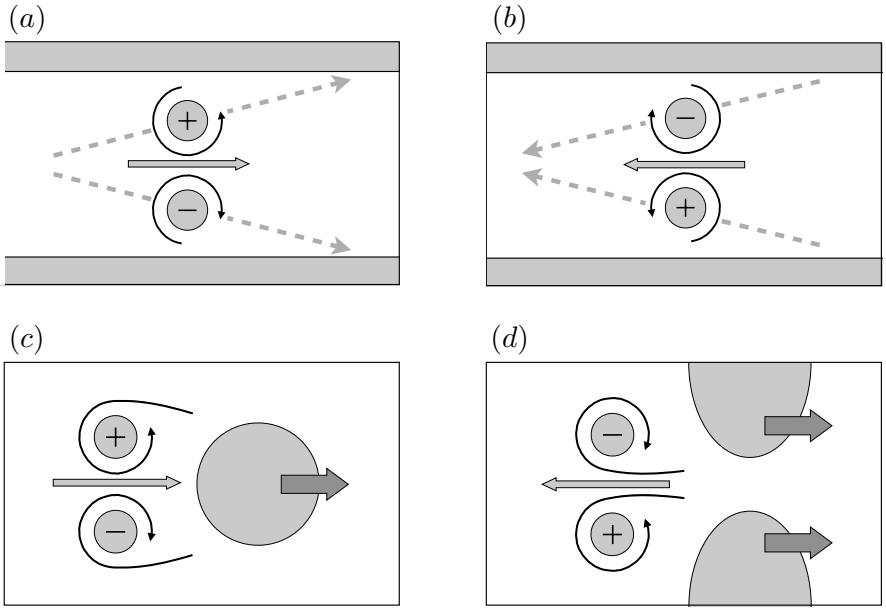

Figure 2.1: Two ways in which positive x direction momentum may be transferred to a trapped condensate via vortex dipoles. A dipole may separate and the vortices move to the boundary and annihilate, introducing positive x direction momentum to the system (a), or an anti-dipole may contract and annihilate, removing negative x direction momentum from the system (b). A vortex dipole may form behind an obstacle dragged through a superfluid (c), resulting in (a), or a vortex dipole may form behind an aperture dragged through a superfluid, resulting in (b).

where n is a signed integer, and thus we define the quantum of winding to be $\kappa = 2\pi\hbar/m$. If the contour is such that it only contains a single vortex, then we call n the *charge* of the vortex. A vortex is only stable for $n = \pm 1$; higher charged vortices will quickly decay into multiple singly-charged vortices [13].

Due to the definition of the velocity as proportional to the gradient of the phase, the vorticity is then the curl of a gradient, which is identically zero anywhere the phase is defined. The only points at which the phase is undefined is at the core of vortices where the particle density is zero, and so the vorticity of the condensate is

$$\boldsymbol{\omega}(\mathbf{x}) = \nabla \times \mathbf{v} = \hat{z}\frac{\hbar}{m} 2\pi \sum_{i=0}^{N} n_i \delta(\mathbf{x} - \mathbf{x}_i) \tag{2.38}$$

where N is the number of vortices in the condensate, $\mathbf{x}_i$ is the location of the ith vortex, and n_i is its charge. This is an important difference from classical fluids where $\omega(\mathbf{x})$ is continuous and non-singular, demonstrating the irrotational flow of the quantum fluid.

Oppositely charged vortices can pair to form a vortex dipole, which acts as a carrier of linear momentum. The magnitude of the momentum carried by a vortex dipole is dependent on the distance separating the vortices, and thus annihilation or separation of vortices can introduce or remove linear momentum from the condensate, as shown in Figures 2.1a and 2.1b. The direction of the momentum contained in a vortex dipole is dependent on its orientation.

It has been found that dragging a laser beam through a condensate causes vortex dipoles to be shed off behind the beam [9], as shown in Figures 2.1c and 2.1d.

In an inhomogeneous system, areas where the condensate density is insignificant may

be considered a *vortex reservoir*, and we consider vortices that move to these areas to have annihilated with vortices contained in the vortex reservoir. Vortices close to the boundary of a condensate may experience interactions with vortices in the vortex reservoir.

The structure of vortices forming behind an obstacle in a superfluid has been studied for both subsonic and supersonic obstacle velocities [14].

Under certain conditions, it has been shown that a phenomena analogous to the Bénard-von Kármán vortex street in classical fluids can occur when an obstacle is dragged through a superfluid [15]. This consists of periodic shedding of pairs of like-charged vortices.

2.2.5 Healing Length and Speed of Sound

In the presence of a perturbation, there is a characteristic length from the perturbation where the condensate will have returned to its unperturbed state. We call this length the healing length, and it is defined by

$$\xi(\mathbf{x}) = \frac{\hbar}{\sqrt{mg\rho(\mathbf{x})}} \tag{2.39}$$

where $\rho(\mathbf{x})$ is the local density of the condensate. For homogeneous systems the healing length is a constant of the system, whereas for an inhomogeneous (trapped) system this value is spatially dependent. The healing length can be considered a measure of the size of a vortex core. We can also define the speed of sound in a condensate [8] as

$$c(\mathbf{x}) = \sqrt{\frac{\rho(\mathbf{x})g}{m}} \tag{2.40}$$

which is also constant for homogeneous systems but spatially dependant for inhomogeneous systems; in that case the value corresponding to the peak density is typically used.

Evidently the healing length and speed of sound are related by

$$\xi(\mathbf{x})c(\mathbf{x}) = \frac{\hbar}{m}, \tag{2.41}$$

a useful relation as the right-hand side is independent of both space and time.

The speed of sound can also be defined by

$$\mu(\mathbf{x}) = mc^2(\mathbf{x}) = g\rho(\mathbf{x}) \tag{2.42}$$

where μ is the chemical potential of the condensate. Again, the value at the peak condensate density is typically used for inhomogeneous systems.

2.2.6 Quantum Reynolds Number

The classical definition of the Reynolds cannot be used for quantum fluids, as the kinematic viscosity is, by definition, zero. However the concept can be extended to quantum fluids, and several definitions for a quantum Reynolds number do exist. One definition suggested uses the *kinematic quantum viscosity* [16], which is related to the dimensionless damping rate γ of the system [17] by

$$\nu_q \equiv \frac{\hbar\gamma}{2m} \tag{2.43}$$

giving a quantum Reynolds number of

$$Re_s = \frac{UL}{\gamma}\frac{2m}{\hbar}, \tag{2.44}$$

where the subscript s indicates that we are referring to the Reynolds number for a superfluid. The constant γ is the rate of scattering between particles in the condensate and atoms in the non-condensate thermal cloud; this is discussed in more detail in section 4.1.2.

Motivated by the fundamental role of vortices in turbulent flows, Volovik [18] suggested that the quantum Reynolds number should be written as

$$Re_s = \frac{UL}{\kappa} \tag{2.45}$$

where U is now the relative superfluid velocity and L is again a characteristic length.

The former may apply in an appropriate classical limit, while the latter seems more appropriate for smaller systems.

Any values given in this work for a quantum Reynolds number have been calculated using Volovik's definition, for our small systems.

2.3 Persistent Currents: Formation and Decay

In this section we introduce the concepts of *persistent currents* and *critical velocities*, in the context of decaying persistent currents. We also briefly discuss previous works that have investigated the formation, stability, and decay of persistent currents, both experimentally and numerically.

2.3.1 Persistent Currents

If Ψ denotes the ground state of a periodically trapped condensate (such as in Figure 2.2), then, under certain conditions, a transformation of the form

$$\Psi \to \Psi e^{i\theta(\mathbf{x})} \tag{2.46}$$

can give a metastable state, for certain $\theta(\mathbf{x})$. The velocity field in the condensate is then given by equation (2.36), and we say that the state has a persistent current. The condition for the transformation to exist is that $\theta(\mathbf{x})$ satisfies equation (2.37) for some integer n when the contour integral is around the entire period of the system. This condition ensures that the velocity of persistent currents is quantised. A persistent current must enclose a phase singularity, and this manifests as a central vortex of charge n in the condensate.

Since the new state corresponds to the ground state moving with some velocity $\mathbf{v}(\mathbf{x}) = \frac{\hbar}{m}\nabla\theta(\mathbf{x})$, we may write it as

$$\Psi_{\mathbf{v}}(\mathbf{x}, t) = \Psi_o(\mathbf{x} - \mathbf{v}t, t) \tag{2.47}$$

where a subscript o denotes the original state, and a subscript $\mathbf{v}$ denotes the same state travelling at the (constant) fluid velocity $\mathbf{v}$. We say we have 'boosted' the state $\Psi_o(\mathbf{x}, t)$. Since $\Psi_o(\mathbf{x}, t)$ satisfies the Gross-Pitaevskii equation (2.18) in the lab frame, it follows that $\Psi_{\mathbf{v}}(\mathbf{x}, t)$ satisfies

$$i\hbar\partial_t\Psi_{\mathbf{v}}(\mathbf{x}, t) = \left[\frac{1}{2m}\left(i\hbar\nabla + m\mathbf{v}\right)^2 - \frac{mv^2}{2} + V_{\text{trap}}(\mathbf{x} + \mathbf{v}t) + g|\Psi_{\mathbf{v}}(\mathbf{x}, t)|^2\right]\Psi_{\mathbf{v}}(\mathbf{x}, t) \tag{2.48}$$

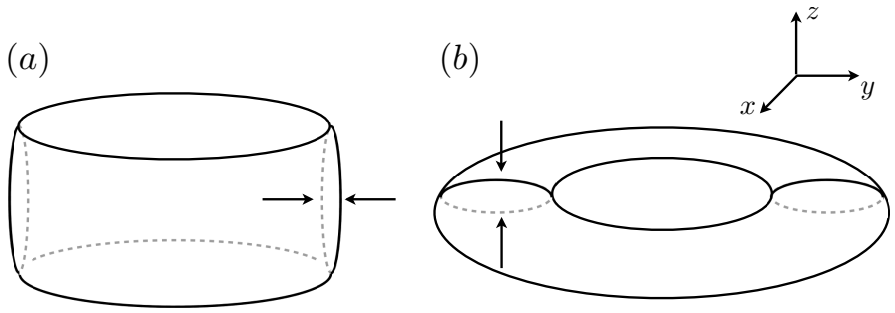

Figure 2.2: Trapping potentials that can support persistent currents in confined quasi-two-dimensional Bose-Einstein condensates. The non-trivial topology of the toroid provides the pinning for the central vortex. In (a) the radial dimension is tightly confined, and thus the trap may be represented by a linear two-dimensional tube with periodic boundary conditions. In (b) the vertical dimension is tightly confined, however the trap may still be approximated by a linear two-dimensional tube with periodic boundary conditions provided the toroidal width is much less than the toroidal radius.

in the moving frame. Applying this with the time-independent forms of the Gross-Pitaevskii equation tells us that if $\Psi_o(\mathbf{x}, t)$ is the ground state in the lab frame with chemical potential μ_o, then $\Psi_{\mathbf{v}}(\mathbf{x}, t)$ is the ground state in the fluid frame with the same chemical potential μ_o, but with the acquired phase factor $e^{i\theta(\mathbf{x})}$.

It has been shown analytically that a harmonically trapped Bose-Einstein condensate will not support a persistent current, due to the instability of quantum vortices [19]. Only if the central vortex is 'pinned' in place can the condensate support a persistent current. The condensate must be contained in a trap with non-trivial topology; if a vortex is imprinted on a harmonically trapped condensate, the central vortex will simply decay to the condensate boundary, causing the current to decay to zero.

It was suggested [20] that a toroidal trap, as in Figure 2.2, would provide the 'pinning' of the central vortex such that a persistent current could be supported. A method of creating a persistent current from a ground state in one dimension was also suggested, using a time-dependent stirring potential. In this paper the toroid was approximated as a linear channel with periodic boundary conditions, a valid approximation provided the toroidal radius is much larger than the trap width, which certainly applies in the case of a one-dimensional condensate.

Persistent currents were first observed experimentally in 2007 by Ryu et al [4], who created a persistent current by transferring one unit of angular momentum using Laguerre-Gauss beams [21] to a toroidally trapped condensate. The current was observed without decay for 10 seconds, limited only by the trap lifetime. They also created a persistent current with two units of angular momentum, and observed the central vortex split into two singly charged vortices when the repulsive trap centre was removed, thus also demonstrating the instability of multiply charged vortices and confirming that a harmonic trap cannot sustain a persistent current.

Ryu et al detected the presence of the persistent current by removing the central 'pinning' beam of the toroidal trap, altering it into a harmonic trap, and then observing that a central vortex remained. If no persistent current were present, then a central vortex would not be observed. Another method of detecting a persistent current was proposed where standing waves in the condensate density are induced [22], before the condensate is released from

the trap, allowing it to expand freely. In the absence of a persistent current, interference due to the standing wave causes a rotationally and axially symmetric 'petal' pattern. If a persistent current is present, the pattern is distorted such that axial symmetry is broken and only rotational symmetry remains. Both these methods have the disadvantage that they are destructive. A non-destructive method of detecting persistent currents has been suggested [23] by measuring changes in the condensate density in the presence of an adiabatically introduced (and later removed) probe beam.

A method of creating a persisting current has been suggested [24] wherein the condensate is initially trapped in an optical ring lattice. The lattice can then be rotated, and adiabatically altered into a toroid, resulting in a toroidal trap containing a rotating condensate. Thus the condensate would then be supporting a persistent current.

2.3.2 Critical Velocities

An important phenomena in superfluid flow is the onset of dissipation. When confined to a periodic trap, a superfluid can support a persistent current even in the presence of defects in the trap, provided the velocity of the fluid is suitably low. More specifically, in the presence of an obstruction or defect there is some critical velocity of the fluid above which dissipation will occur, and the current will decay. This critical velocity is the minimum relative velocity between the superfluid and an obstruction, or the superfluid and its trap, required for excitations to occur, and is in general dependent on the nature of the obstruction. It has been shown that for obstacles in a superfluid flow, the fluid 'sees' the obstacle as being larger than it really is. This means the effective obstacle sizes are increased [25], and thus even obstacles with sizes less than one healing length give rise to a finite critical velocity. It should be noted that this is not unique to current decay; the obstruction or trap could be moved relative to a stationary superfluid, and the same phenomena of dissipation is observed [26]. These two systems are connected by a Galilean transformation.

Landau Critical Velocity

In his seminal work into the superfluidity of helium II, Landau considered the situation of flow through a capillary [27]. In the fluid frame, with the capillary moving at $-\mathbf{v}$, for an excitation to occur the energy of the fluid must be greater than or equal to the energy of the excitation $\varepsilon(\mathbf{p})$, where $\mathbf{p}$ is the momentum of the excitation. Performing the well know Galilean transformation of energy and momentum into the capillary frame leads to the energy in this frame

$$E = \varepsilon(\mathbf{p}) + \mathbf{p}\cdot\mathbf{v} + \frac{mv^2}{2}. \tag{2.49}$$

The last term is simply the initial kinetic energy of the flowing fluid, and thus the first two terms are the change in energy due to the excitation. This must be negative since the energy of the flowing liquid must decrease. That is,

$$\varepsilon(\mathbf{p}) + \mathbf{p}\cdot\mathbf{v} < 0, \tag{2.50}$$

and thus the *Landau critical velocity* is given by

$$v_L = \min_{\mathbf{p}} \frac{\varepsilon(\mathbf{p})}{|\mathbf{p}|}. \tag{2.51}$$

The value of the critical velocity then depends on the nature of the lowest energy elementary excitations. For a weakly-interacting system with a Bogoliubov excitation spectrum, the elementary excitations are phonons with energy $\varepsilon(\mathbf{p}) = c\mathbf{p}$. This leads to a Landau critical velocity of $v_L = c$, the speed of sound in the system. We note that Landau was considering the properties of a homogeneous, incompressible superfluid, and thus for an inhomogeneous, compressible superfluid (such as a trapped Bose-Einstein condensate) the Landau critical velocity tends to be an upper bound on the true critical velocity. The condition that the local velocity exceeds the local speed of sound somewhere in the fluid is often referred to as the Landau criterion.

Using perturbation theory, an analytic expression was found [28] for the critical velocity in one dimension. It was shown that, in this case, Landau's criterion failed, but it was concluded that this was probably due to the essential one dimensional physics of the model.

Using hydrodynamical arguments, Frisch et al [26] derived a critical velocity for stable flow around a cylinder. By applying the Landau criterion locally at the cylinder boundary, it was estimated that the critical velocity of the incident flow should be $(\frac{2}{11})^{1/2}c$. This agreed with their numeric results for flow incident on an ideal cylinder of one particular size. While this agrees with experiments in that it is less than the local speed of sound, it does not predict variation of the critical velocity with variation of the obstacle size (or shape), which could be problematic.

Critical values for meeting the Landau criterion have been investigated for various potentials in one dimension [23]. In this case, the critical values investigated were not for the critical velocity, but for the critical value of the ratio between interaction energy and kinetic energy in the condensate.

Feynman Critical Velocity

In his set of lectures on statistical mechanics, Feynman considered the situation of superfluid flowing out of a channel into a reservoir of fluid at rest. Excitations for this scenario were proposed to be vortex-anti-vortex lines nucleating from the edges of the channel [29]. Energy considerations for this scenario then lead to the *Feynman critical velocity*

$$v_F = \frac{\hbar}{mD} \ln\left(D/\xi\right) \tag{2.52}$$

where D is the annular width of the channel. This is generally significantly lower than the value given by the Landau critical velocity.

Ramanathan et al [30] stimulated current decay in a toroidally trapped system by the introduction of an optical barrier, and found the critical velocity falling between upper and lower estimates of the Feynman critical velocity, to within experimental error. Piazza et al [31] considered the system of [30] using a Gross-Pitaevskii model, finding that the Feynman critical velocity is in general much lower than the critical velocity predicted by simulations. Mathey et al [32] also simulated the experiment of [30] using a numerical implementation of the truncated Wigner approximation, comparing the results to both the experiment results and results from a Gross-Pitaevskii model. They found that the Wigner approach gave values closer to the experiment results than the Gross-Pitaevskii model, although still not with complete agreement, concluding that thermal fluctuations have an important role.

It seems likely that for finite systems there are a significant amount of additional physical effects.

2.4 Topic of this Thesis

In this work we investigate the decay of a persistent current in a periodically trapped Bose-Einstein condensate, using the hybrid Lagrangian variational method adaptation of a Gross-Pitaevskii model to allow modelling of less anisotropic systems.

We simulate condensates supporting persistent currents confined to a toroidal trap. The current decay is stimulated in one of three different ways:

1) We create dipoles in the condensate, which annihilate or polarise to remove linear momentum.

2) We introduce a Gaussian obstacle, replicating the process in Figure 2.1c in the frame of the obstacle.

3) We introduce an aperture, replicating the process in Figure 2.1d in the frame of the aperture.

The obstacle describes the persistent current being obstructed by a laser beam in the lab frame, or stirred with a laser beam in the fluid frame. The aperture describes the persistent current being obstructed by a combination of laser beams in the lab frame, or stirred with a combination of laser beams in the fluid frame. The aperture and obstacle are contrasting types of obstruction.

We derive the hybrid Lagrangian variational method equations of motion, and analyse the solutions produced by solving them in their damped form. We investigate current decay in the absence of any obstructions by imprinting dipoles on a state containing a persistent current. We systematically investigate the current decay process for a range of aperture and obstacle sizes, and initial current velocities.

2.5 Summary

In this chapter we have discussed some of the basics of classical fluid dynamics. We have then introduced quantum fluid dynamics and discussed some important concepts in that area. We then introduced two phenomena in quantum fluids that are particularly important to this work. During this we have also discussed previous research done in this area. In the next chapter we outline the numerical essentials necessary for this work.

Chapter 3

Numerical Essentials

3.1 Dimensionless Formalism

When performing computations involving very small numbers, as frequently occur in quantum mechanical systems, it is important to realise that the machine accuracy may affect the results. The machine used to run simulations in this case has a machine accuracy of $\epsilon \approx 2 \times 10^{-16}$, which is larger than multiple parameters in our system, including but not limited to the mass of the particles and the value of $\hbar$. Thus it is important to recast our equations of motion in a dimensionless form with parameters closer to unity, to avoid machine error. In a homogeneous condensate the natural choice for a length unit is the healing length ξ, and for a velocity unit the speed of sound in the condensate c. Together these also define a time unit of ξ/c. The natural unit of energy is the chemical potential μ. We can also apply these units to trapped systems, where the units are defined as the values at the peak condensate density. Thus our dimensionless units are:

$$\tilde{x} = x/\xi \qquad \tilde{v} = v/c \qquad \tilde{t} = t/(\xi/c) \qquad \tilde{E} = E/\mu \tag{3.1}$$

where a tilde represents a dimensionless unit. We also need to rescale the wavefunction so that

$$\int |\Phi|^2 d^2\mathbf{x} = \int |\tilde{\Phi}|^2 d^2\tilde{\mathbf{x}} = N \tag{3.2}$$

which results in

$$\tilde{\Phi} = \xi\Phi. \tag{3.3}$$

By substituting these into the HLVM equations of motion, we obtain their dimensionless form

$$\left[-\frac{1}{2}\left(\frac{\partial^2}{\partial\tilde{x}^2} + \frac{\partial^2}{\partial\tilde{y}^2}\right) + \tilde{V}_{||} + \frac{\tilde{g}}{\sqrt{2\pi}\tilde{w}}|\tilde{\Phi}|^2\right]\tilde{\Phi} = i\frac{\partial\tilde{\Phi}}{\partial\tilde{t}} \tag{3.4}$$

and

$$\ddot{\tilde{w}} + \tilde{\omega}_z^2\tilde{w} = \frac{1}{\tilde{w}^3} + \frac{\tilde{g}\tilde{U}_{||}}{\sqrt{2\pi}N\tilde{w}^2}. \tag{3.5}$$

The 'tube' trapping potential has the dimensionless form

$$\tilde{V}_{||} = \frac{1}{2}\tilde{\omega}_y^2\tilde{y}^2, \tag{3.6}$$

where $\omega_y = \tilde{\omega}_y(\xi/c)$. The dimensionless interaction parameter is

$$\tilde{g} = \frac{g}{\mu\xi^3}, \tag{3.7}$$

and we note that μ is constrained to be 1 in dimensionless units since it is the unit of energy. The value of the dimensionless interaction parameter is then determined solely by the trap geometry and the total particle number.

Another set of characteristic units we could have chosen for a trapped system is given by the harmonic oscillator units, where the length is the harmonic oscillator length $l = \sqrt{\hbar/m\omega_z}$, the unit of energy is the harmonic oscillator energy $\hbar\omega_z$, and the unit of time is ω_z^{-1}. The units we have chosen are natural for a homogeneous system.

3.2 Simulation Parameters

3.2.1 System Size

We choose for our simulations values found for rubidium-87, as this is commonly used for creating Bose-Einstein condensates. Other possible species include sodium-23 [33] or lithium-7 [34]. The number of particles in the condensate is $N = 10^5$. The healing length of the condensate is $\xi = 0.114$ μm, and the speed of sound is $c = 6.4$ mm/s. This gives for the dimensionless time unit $t_o = \xi/c = 0.0177$ s. The chemical potential of the system is $\mu/k_B = 428$ nK. In Table 3.1 we show some parameters from experiments on real systems.

We choose a spatial system size of $L = (160\xi)^2 = (18.3\ \mu\text{m})^2$. The relatively small system allows us to use a manageable grid size while maintaining appropriate spatial resolution, thus speeding up numerical calculations. We choose a trapping of $\omega_y = 0.0354c/\xi = 215\times 2\pi$ Hz to obtain a Thomas-Fermi radius for the condensate of $R_y = 40\xi = 4.5$ μm. In our dimensionless units the inter-particle interaction strength is $g = 0.58\mu/\xi^3$. The Thomas-Fermi Gaussian thickness of the condensate is $w_o = 2.73\xi$, compared to the harmonic oscillator length of $l_z = 1.68\xi$; this significant difference supports our used of the hybrid Lagrangian variational method over the traditional Gross-Pitaevskii model. We choose the anisotropy of the system to be $\lambda = \omega_z/\omega_y = 10$, much lower than is traditional for simulating quasi-two-dimensional systems; for example, in [35] the anisotropy used was on the order of $\lambda \sim 100$.

Table 3.1: Values of the healing length (ξ), speed of sound (c), chemical potential (μ), condensate particle number (N), and anisotropy (λ) taken from a small selection of experimental papers on persistent currents. Also shown are the values used in this work for comparison.

Paper	ξ (μm)	c (m/s)	μ/k_B (nK)	N	λ
Ryu *et al* [4]	0.606	0.0064	58.5	3×10^5	5
Onofrio *et al* [36]	0.235	0.0012	3.98	$2-5\times10^5$	$1.42-2.04$
Ramanathan *et al* [30]	0.195	0.0070	135	1.8×10^7	~ 1
This Work	0.114	0.0064	428	1×10^5	10

3.2.2 Varying Parameters

We position the stirrer in the centre of the channel, where the condensate density is at its peak. The parameters we vary are the obstacle width S_o, or the aperture width S_a, and the initial winding of the system n. All the windings we use give a velocity less than the speed of sound. We choose to work with a fixed stirrer strength of $V_o = 2\mu$. Because the stirrer strength is greater than the chemical potential, the stirrer is impenetrable, meaning the condensate density goes to zero for $r \lesssim S_o/2$. The stirrer is always centred on the x-axis at $x_o = -60\xi$. In real systems, the obstacle corresponds to a blue-detuned laser with a Gaussian transverse profile. The aperture potential is more complex as it involves functions other than Gaussians, however it has been shown that complex dynamic trapping potentials for Bose-Einstein condensates can be created experimentally [37].

3.2.3 Damping

The damping coefficient is phenomenological, and thus we are unable to attribute to it a corresponding temperature. We are interested in the qualitative behaviour of our systems, and thus we use a relatively high value of the damping coefficient. This also decreases the time scale for decay to occur. We use a value for the dimensionless damping coefficient of $\gamma = 0.03$ unless otherwise indicated, a high value compared to those in experiments, which are typically on the order of $\gamma \sim 10^{-4}$. However, γ remains the smallest parameter in the system and will give the correct phenomenology. In some cases we may compare this to a system in the absence of damping.

3.3 Numerical Convergence

The algorithm used in this work to solve the HLVM equations of motion is an adapted version of the Fourth-Order Runge-Kutta in the Interaction Picture (RK4IP) algorithm. A detailed description of this algorithm can be found in [38].

Because a portion of the RK4IP algorithm involves transformation to the interaction picture, the algorithm transforms the wavefunction to Fourier space and back several times per iteration. Thus we need to ensure that the grid sizes used give adequate spatial resolution, as this affects the wavenumber range in Fourier space. We must also check that the time steps used are sufficiently small for the parameters we consider.

We investigate the effects of varying grid size and and time step size for a particular set of system parameters. We choose the parameters for which current decay is first observed, and also the most extreme parameters used. We initially choose a grid size of $M = (512)^2$ and a step size of $\Delta t = 0.1(\xi/c) = 0.1t_o$. We set the Thomas-Fermi radius of the condensate to 40ξ and use a system size of $L = (160\xi)^2$, giving a spatial resolution of 10.2 points per square healing length. In most applications, a resolution of ≈ 3 points per square healing length is sufficient [35]

We always choose grid sizes to be powers of 2, since FFT algorithms are more efficient with such grid sizes. We investigate the effect of using coarser or finer grids and larger or smaller time steps by calculating the rate of change of linear momentum of the system due to forcing for each case. The parameters we use this for are chosen such that the system dynamics are the most strongly non-equilibrium that we look at, and involve the highest energies. The

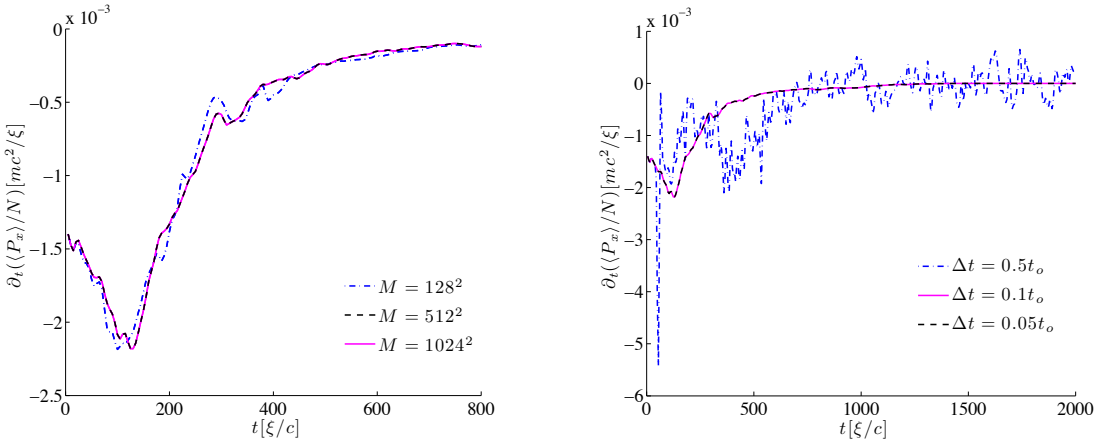

Figure 3.1: The effects of varying grid size and tolerance on the rate of change of linear momentum for the parameters $n = 20$ ($v_i = 0.7854$) and obstacle size $S_o = 12\sqrt{2}$. We can see that increasing the grid size to $M = 1024^2$ does not appreciably affect the results, and so a grid size of $M = 512^2$ is sufficient. Decreasing the time step size also does not appreciably affect the results, so our time step of $\Delta t = 0.1t_o$ is sufficient. Lowering the grid size or increasing the time step size adversely affects the numerical convergence.

findings are presented in Figure 3.1, where we can see that a grid size of $M = 512^2$ and a step size of $\Delta t = 0.1t_o$ are sufficient for numerical convergence of our simulations.

3.4 Vortex Detection

Vortices are detected in the simulations using the fact that the vorticity of the system is zero except at a vortex core, the curl-free condition of superfluidity. That is, in two-dimensional systems, the vorticity is the scalar

$$\omega = (\nabla \times \mathbf{v})_z \propto \delta^2(\mathbf{x} - \mathbf{x}_i) \tag{3.8}$$

where $\mathbf{x}_i$ is the location of the vortex core. Finding the vorticity of the numerical system gives a signal at the vortex core and a few neighbouring grid points, which are averaged over. Positive and negative vortices can be distinguished by the sign of the signal. To exclude the many insignificant vortices residing in the low-density areas outside of the trap, a mask is applied to the system out to the Thomas-Fermi radius before the vortex detection algorithm is applied. The algorithm is accurate to within the grid resolution $\Delta x = 0.3125$.

3.5 Computational Requirements

All simulations were performed on a machine with processing delivered by a 6 core Intel Core i7-3930K 3.82GHz processor, and 64GB of physical memory. All coding was written in the MATLAB programming language. Due to storage constraints, data files had to be smaller than 5GB. Data file sizes ranged from the order of 50MB to 5GB, while total data storage requirements were on the order of 100GB.

Chapter 4

Results

In this chapter we present our results from investigating persistent current decay using the hybrid Lagrangian variational method. We first present a derivation of the hybrid Lagrangian equations of motion, as well as some investigation into its accuracy. We then briefly explore the properties of dipole decay in a linear trap in the absence of obstructions. After this we present the results of our primary investigation into the decay of a persistent current in the presence of an obstacle or aperture, as modelled by the hybrid Lagrangian variational method. Finally, we present some comparisons between the decay induced by an obstacle and that induced by an aperture.

4.1 The Hybrid Lagrangian Variational Method

The method we used was taken from Edwards et al [10]. However the derivation in this was done in dimensionless units, that differ from the units we have chosen. Thus we re-derive the equations of motion starting with the dimensional Lagrangian density to find them in their dimensional form. We also do some comparisons to Thomas-Fermi descriptions to gauge their accuracy.

4.1.1 Formulation

The three-dimensional time-dependent Gross-Pitaevskii equation (3D TDGPE) is a variational equation of motion that may be derived from the Lagrangian density

$$\begin{aligned}\mathcal{L}[\Psi] =& \frac{1}{2}i\hbar(\Psi\Psi_t^* - \Psi^*\Psi_t) + \frac{\hbar^2}{2m}\sum_{\eta=x,y,z}\Psi_\eta^*\Psi_\eta \\ &+ V_{\text{trap}}(\mathbf{x})\Psi^*\Psi + \frac{1}{2}g(\Psi^*)^2(\Psi)^2, \end{aligned} \tag{4.1}$$

where m is the mass of the atom species in the condensate, g is the inter-particle interaction given by equation (2.15), and $\Psi_\eta \equiv \partial_\eta\Psi$. The Euler-Lagrange equation that produces the 3D TDGPE from this Lagrangian density is

$$\sum_{\eta=x,y,z,t}\frac{\partial}{\partial\eta}\left(\frac{\partial\mathcal{L}}{\partial\Psi_\eta^*}\right) - \frac{\partial\mathcal{L}}{\partial\Psi^*} = 0. \tag{4.2}$$

We may consider this to be one limit of the Lagrangian variational method, wherein the wavefunction is a completely unspecified function. The other limit is where the functional form of the wavefunction is completely specified $\Psi(\mathbf{x},t) = \psi(\mathbf{x}; q_1, ..., q_n)$, and the time-dependence is contained in the n time-dependent variational parameters $q_1(t), ..., q_n(t)$. Applying the usual Euler-Lagrange equations results in n differential equations for the variational parameters which are, in general, coupled. The hybrid Lagrangian variational method then lies midway between these two limits, assuming a wavefunction where one component is specified functionally, while the other is completely unspecified. We take this approach, writing the wavefunction as

$$\Psi(x,y,z,t) = \bar{\Phi}(x,y,t)A(t)e^{-z^2/2w^2(t)+i\beta(t)z^2}, \tag{4.3}$$

and assume that the potential is of the form

$$V(\mathbf{x}) = V_{||}(x,y) + \frac{1}{2}m\omega_z^2 z^2. \tag{4.4}$$

The z dimension profile is thus assumed to be a Gaussian, with the Gaussian width $w(t)$ and a quadratic phase factor $\beta(t)$. Normalisation constraints give $A(t) = (\sqrt{\pi}w(t))^{-1}$. Inserting this wavefunction into the Lagrangian density and integrating over the z dimension gives the *hybrid* Lagrangian density

$$L_{hybrid}[\bar{\Phi}, w, \beta] = \int_{-\infty}^{\infty} \mathcal{L}[\bar{\Phi}Ae^{-z^2/2w^2+i\beta z^2}]dz. \tag{4.5}$$

The Euler-Lagrange equations to apply are now

$$\frac{\partial L_{hybrid}}{\partial w} - \frac{\partial}{\partial t}\left(\frac{\partial L_{hybrid}}{\partial \dot{w}}\right) = 0, \qquad \frac{\partial L_{hybrid}}{\partial \beta} - \frac{\partial}{\partial t}\left(\frac{\partial L_{hybrid}}{\partial \dot{\beta}}\right) = 0, \tag{4.6}$$

and

$$\frac{\partial}{\partial x}\left(\frac{\partial L_{hybrid}}{\partial \bar{\Phi}^*_x}\right) + \frac{\partial}{\partial y}\left(\frac{\partial L_{hybrid}}{\partial \bar{\Phi}^*_y}\right) - \frac{\partial L_{hybrid}}{\partial \bar{\Phi}^*} = 0. \tag{4.7}$$

The first gives

$$\left[-\frac{\hbar^2}{2m}\left(\frac{\partial^2}{\partial x^2} + \frac{\partial^2}{\partial y^2}\right) + V_{||} + g_e|\bar{\Phi}|^2\right]\bar{\Phi} = i\hbar\frac{\partial \bar{\Phi}}{\partial t} - \hbar F(t)\bar{\Phi} \tag{4.8}$$

where $g_e(t)$ is given by equation (2.15), and

$$F(t) = \frac{1}{2}\dot{\beta}w^2 + \frac{\hbar}{m}\beta^2 w^2 + \frac{\hbar}{4m}\frac{1}{w^2} + \frac{1}{4\hbar}m\omega_z^2 w^2. \tag{4.9}$$

We eliminate $F(t)$ by making the transformation

$$\bar{\Phi}(x,y,t) \equiv \Phi(x,y,t)e^{-i\hbar\int_0^t F(t')dt'}. \tag{4.10}$$

Substituting this into equation (4.8) gives us the Gross-Pitaevskii equation

$$\left[-\frac{\hbar^2}{2m}\left(\frac{\partial^2}{\partial x^2} + \frac{\partial^2}{\partial y^2}\right) + V_{||} + g_e|\Phi|^2\right]\Phi = i\hbar\frac{\partial \Phi}{\partial t} \tag{4.11}$$

and we note that the spatial independence of the additional phase means that the transformation does not affect the essential physics of the system dynamics, it is just a convenient energy shift. Thus we need only solve for Φ, not $\bar{\Phi}$.
Applying the second Euler-Lagrange equation and integrating over x and y gives a relationship between β and w

$$\beta = \frac{m\dot{w}}{2\hbar w}, \tag{4.12}$$

which, with the aforementioned transformation, allows us to eliminate β from the equations of motion.
Applying the third Euler-Lagrange equation, integrating over x and y, and exploiting the relationship in equation (4.12) gives the Gaussian width equation

$$\ddot{w} + \omega_z^2 w = \frac{\hbar^2}{m^2}\frac{1}{w^3} + \frac{g_e}{mwN}U_{||}. \tag{4.13}$$

where $U_{||}$ is given by

$$U_{||}(x,y,t) = \int d^2\mathbf{x}|\Phi(x,y,t)|^4. \tag{4.14}$$

4.1.2 Damping Form

We introduce a phenomenological dimensionless damping coefficient [17] to the HLVM equations of motion to simulate the system being coupled to a thermal cloud with a specified temperature T and chemical potential μ. This constant is extracted from damped Gross-Pitaevskii theory [16], and is defined by

$$\gamma = \frac{4mk_BTa^2}{\pi\hbar^2} = \frac{8a^2}{\lambda_{dB}^2} \tag{4.15}$$

where k_B is the Boltzmann constant, T is the temperature, and λ_{dB} is the thermal de Broglie wavelength

$$\lambda_{dB} = \sqrt{\frac{2\pi\hbar^2}{mk_BT}}. \tag{4.16}$$

Damped Gross-Pitaevskii theory is a derivative of the stochastic projected Gross-Pitaevskii model without considering noise. The damping is due to collisions between atoms in the ground state (that is, in the condensate) and atoms in excited states.

The damped HLVM equations of motion are

$$i\hbar\frac{\partial\Phi(x,y,t)}{\partial t} = (\mathscr{L} - \mu)(1 - i\gamma)\Phi(x,y,t), \tag{4.17}$$

where

$$\mathscr{L}\Phi(x,y,t) = \left[-\frac{\hbar^2}{2m}\left(\frac{\partial^2}{\partial x^2} + \frac{\partial^2}{\partial y^2}\right) + V_{||}(x,y) + g_e(t)|\Phi(x,y,t)|^2\right]\Phi(x,y,t), \tag{4.18}$$

and

$$\ddot{w} + \gamma\dot{w} + \omega_z^2 w = \frac{\hbar^2}{m^2}\frac{1}{w^3} + \frac{g_e}{mwN}U_{||}. \tag{4.19}$$

The term $\gamma\dot{w}$ is justified by noting the similarity between equation (4.13) and the standard equation for a driven harmonic oscillator

$$\ddot{x} + \omega^2 x = F(x,t). \tag{4.20}$$

The usual way to include damping into this model is to include a term like $\gamma\dot{x}$, and thus we do this for our width equation. The inclusion of this term ensures that evolution proceeds toward the correct ground state.
The damped HLVM equations of motion (4.17) and (4.19) are then solved using our RK4IP algorithm.

4.1.3 Potentials

The trap consists of a linear channel of length L with periodic boundary conditions described by the potential

$$V_{||}(x,y) = \frac{1}{2}m\omega_y^2 y^2, \tag{4.21}$$

where ω_y is the trapping frequency. This trap is an approximation of a toroidal trap strongly confined in the z dimension for the case where the toroidal radius is much greater than the trap width, or an exact representation of a toroidal trap strongly confined in the radial dimension, as shown in Figure 2.2. For this trapping potential, the phase factor required to apply a persistent current with winding n is

$$\theta(\mathbf{x}) = \frac{2\pi n}{L}x, \tag{4.22}$$

which gives for the superfluid velocity

$$v_x = \frac{\hbar}{m}\frac{2\pi n}{L}. \tag{4.23}$$

The obstacle is described by the potential

$$V_{\mathrm{ob}}(x,y) = V_o \exp\left(-\frac{(x-x_o)^2}{\sigma^2} - \frac{y^2}{\sigma^2}\right) \tag{4.24}$$

where the obstacle is positioned in the centre of the channel at $(x,y) = (x_o, 0)$. We use for all simulations $x_o = -60\xi$, noting that the origin is at the trap centre. We vary the obstacle width by varying σ.

The aperture is described by the potential

$$V_{\mathrm{ap}}(x,y) = V_o\left[\exp\left(-\frac{(x-x_o)^2}{\sigma_x^2} - \frac{(y-y_o)^4}{\sigma_y^4}\right) + \exp\left(-\frac{(x-x_o)^2}{\sigma_x^2} - \frac{(y+y_o)^4}{\sigma_y^4}\right)\right] \tag{4.25}$$

where the centre of the aperture is positioned on the centre of the channel at $(x,y) = (x_o, 0)$, and the maxima of the aperture potential are positioned at $(x_o, \pm y_o)$. Again we use $x_o = -60\xi$ for all simulations. The aperture potential is Gaussian in the x-dimension, but sharper than that in the y-dimension. This is to ensure that the aperture width is able to be well-defined, and so the aperture potential within the aperture is very close to zero. We vary the aperture width by varying the value of y_o.

For estimating the value of the Feynman critical velocity or quantum Reynolds number, we use an effective width for the obstacle or aperture size, given by where the height falls to its $1/e^2$ value. For the obstacle, this is given by $S_o = 2\sqrt{2}\sigma$. For the aperture, this is given by $S_a = 2\left(y_o - \sqrt[4]{2}\sigma_y\right)$.

4.1.4 The Thomas-Fermi Approximation

It may be impossible to solve the HLVM equations of motion analytically, but an approximation to the solution of the time-independent form may be obtained using the Thomas-Fermi approximation. If the condensate number is very large, then the interaction term in the Gross-Pitaevskii equation dominates over the kinetic energy term wherever the particle density is slowly varying in space, and so we may remove this term from equation (2.29). This can then be easily solved for the condensate density

$$\rho(x,y) = |\phi(x,y)|^2 = \begin{cases} \frac{\mu - V_{||}(x,y)}{g_o} & \text{if } \mu > V_{||}(x,y) \\ 0 & \text{if } \mu \leq V_{||}(x,y). \end{cases} \tag{4.26}$$

The spatial extent of this wavefunction is determined by the Thomas-Fermi radii R_x and R_y, defined by $V_{||}(R_x, R_y) = \mu$. The values of w_o and R_x, R_y are determined by the geometry of the trap. Normalisation of the wavefunction allows us to find a relationship between the chemical potential and the particle number, as well as the chemical potential and $U_{||}$.
We consider the Thomas-Fermi approximation for the case of the tube trap.

The Thomas-Fermi radius is found to be

$$R_y = \sqrt{\frac{2\mu}{m\omega_y^2}} \tag{4.27}$$

in the y dimension; there is no value for the x dimension as the trap is homogeneous in this dimension. The relationship between chemical potential and particle number is then

$$\mu(N) = \left(\frac{3g_o}{4L}\right)^{\frac{2}{3}} \left(\frac{m\omega_y^2}{2}\right)^{\frac{1}{3}} N^{\frac{2}{3}}, \tag{4.28}$$

and the relationship between chemical potential and $U_{||}$ is

$$U_{||}(N) = \frac{16L}{15g_o^2}\sqrt{\frac{2}{m\omega_y^2}}\mu^{\frac{5}{2}}, \tag{4.29}$$

and we note that there is some hidden dependence on N in g_o. Substituting these into the time-independent width equation (2.31) gives us an equation independent of $\phi(x,y)$ that can be solved for the Thomas-Fermi value of w_o

$$\frac{1}{2}m\omega_z^2 w_o^4 - \frac{2}{5}\mu w_o^2 - \frac{\hbar^2}{2m} = 0. \tag{4.30}$$

This is a quadratic in w_o^2, and the solution is, since w_o^2 must be positive,

$$w_o^2 = \frac{\frac{2}{5}\mu + \sqrt{(\frac{2}{5}\mu)^2 + (\hbar\omega_z)^2}}{m\omega_z^2}. \tag{4.31}$$

If we expand the square root and introduce the z dimension harmonic oscillator length $l_z = \sqrt{\hbar/m\omega_z}$ we find that

$$w_o^2 = l_z^2\left[1 + \frac{2\mu}{5\hbar\omega_z} + \frac{1}{2}\left(\frac{2\mu}{5\hbar\omega_z}\right)^2 - \frac{1}{8}\left(\frac{2\mu}{5\hbar\omega_z}\right)^4 + \frac{1}{16}\left(\frac{2\mu}{5\hbar\omega_z}\right)^6 - ...\right] \tag{4.32}$$

and thus we expect that, in the limit that the z dimension harmonic oscillator energy is much greater than the chemical potential, the (stationary) Gaussian width tends toward the harmonic oscillator length l_z. Using this solution for w_o, the stationary value of the interaction strength is then

$$g_o = g_{2D}\left[1 + \frac{2\mu}{5\hbar\omega_z} + \frac{1}{2}\left(\frac{2\mu}{5\hbar\omega_z}\right)^2 - \frac{1}{8}\left(\frac{2\mu}{5\hbar\omega_z}\right)^4 + \frac{1}{16}\left(\frac{2\mu}{5\hbar\omega_z}\right)^6 - ...\right]^{-\frac{1}{2}}, \tag{4.33}$$

and hence we expect g_o to tend towards g_{2D} in the highly anisotropic limit.

4.1.5 Accuracy

We compare tube trap ground states found by using the RK4IP algorithm to ones found by utilising the Thomas-Fermi approximation. To find the ground state numerically, the RK4IP algorithm is used to solve the damped equations of motion with the damping coefficient set to $\gamma = 1$, using the Thomas-Fermi state as the initial approximation; this is equivalent to evolving the Thomas-Fermi approximation state in imaginary time to the true ground state. A direct comparison of the ground state profiles is shown in Figure 4.1. From this we can immediately say that the Thomas-Fermi approximation appears to be extremely good, with the only notable deviation being where the condensate density approaches zero at the condensate edge and near the obstacle. This confirms that the adapted RK4IP code is working and is physically consistent.

We also show in Table 4.1 the Thomas-Fermi values of some system parameters and the same parameters after evolving with unitary damping in the RK4IP algorithm. For each parameter, the difference between the Thomas-Fermi value and the numeric value is less than 1%, indicating that the Thomas-Fermi approximation is indeed very good for this system. Thus the adapted RK4IP algorithm gives the correct ground states.

We expect that, in the limit that the condensate is truly two-dimensional, the Gaussian width w_o should approach the z direction harmonic oscillator length l_z. We compare these for various values of the anisotropy, given by equation (4.32). We can see from Figure 4.2 that w_o does indeed approach l_z for increasing anisotropy, but shows significant variation for lower anisotropy. Also shown is the approximate value of w_o from the first two terms of equation (4.32), which is very close to that given by the full expression. This confirms that, in the limit that the condensate is two-dimensional, we will recover the two-dimensional interaction strength (equation (2.15)) of Gross-Pitaevskii theory, and that using the hybrid Lagrangian variational method for lower anisotropies is justified.

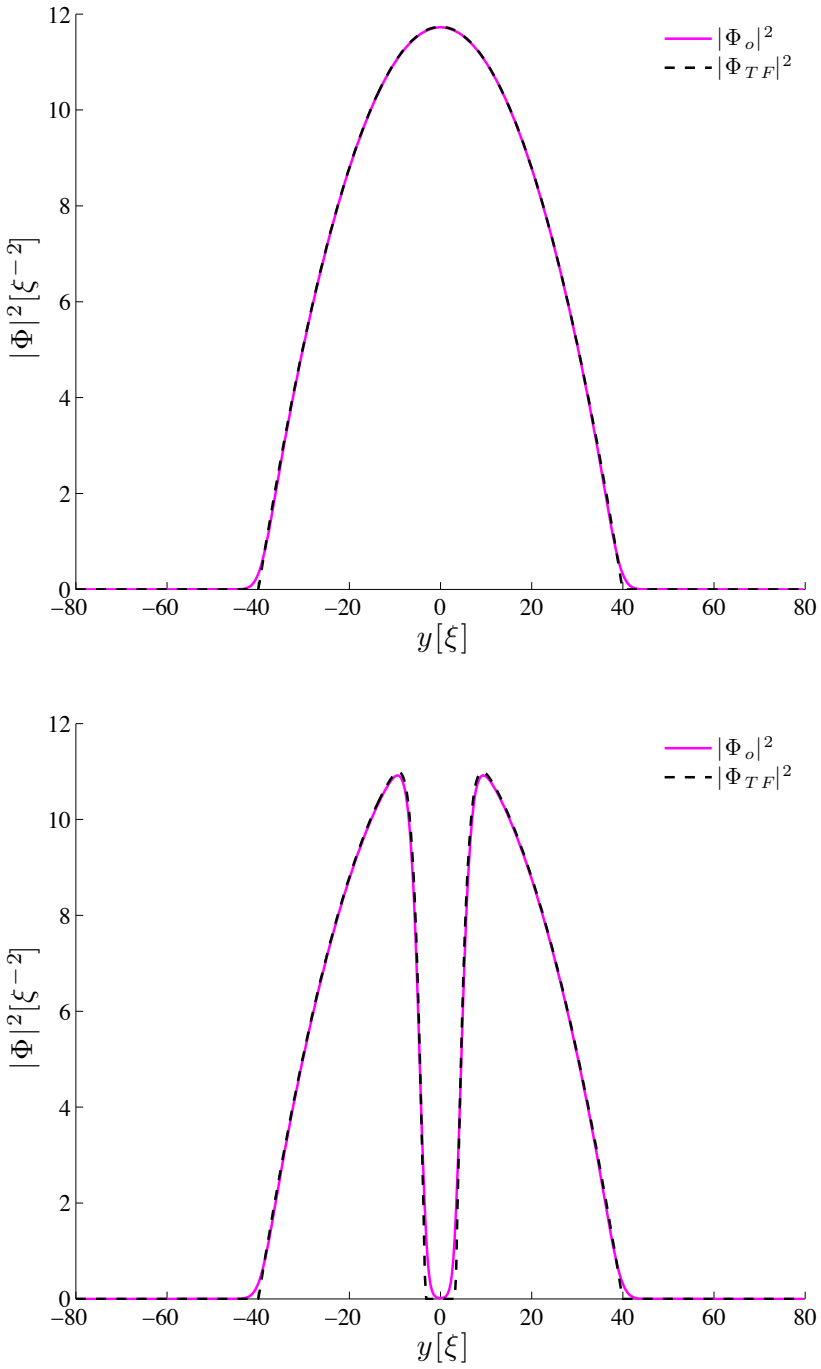

Figure 4.1: Density cross-sections of tube trap ground states given by the Thomas-Fermi approximation and by using the RK4IP algorithm. The top profile is in the absence of any obstacle, and the cross-section is taken through $x = 0$. The bottom profile is in the presence of a Gaussian obstacle of width $S_o = 8\sqrt{2}\xi$, and the cross-section is taken through $x = -60\xi$, which is also where the obstacle is centred. In both cases Φ_o is the numerically obtained ground state and Φ_{TF} is the Thomas-Fermi ground state.

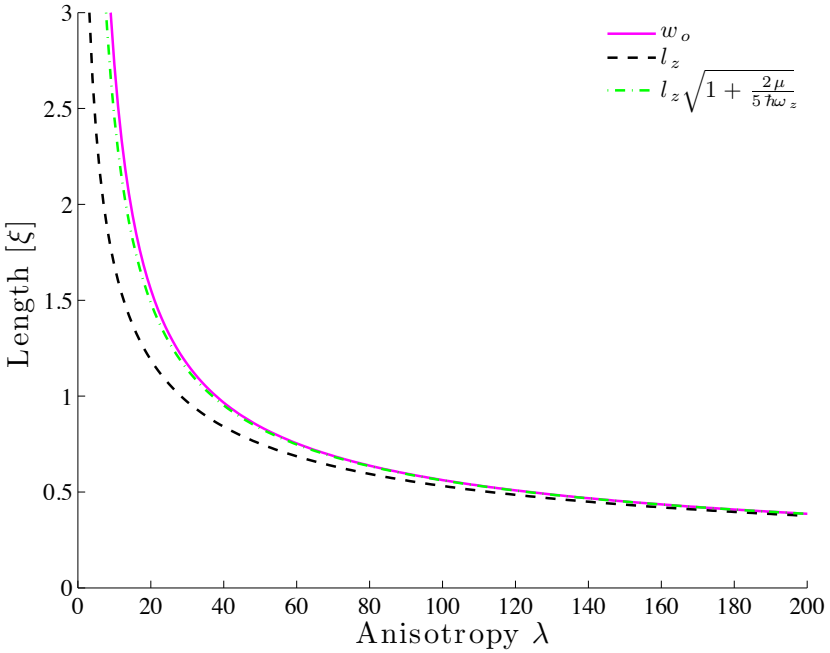

Figure 4.2: Comparison of w_o, the Thomas-Fermi value of the Gaussian width, and l_z, the z direction harmonic oscillator length l_z, as a function of the trap anisotropy. Also shown is the approximate value of w_o as given by the first two terms of equation (4.32).

Table 4.1: Values of the Gaussian thickness of the condensate, $U_{||}$, and the condensate particle number as given by the Thomas-Fermi approximation, compared with the values obtained evolving to a ground state using the RK4IP with unitary damping (numeric value). Also shown is the percentage difference between the Thomas-Fermi values and the numerically obtained values.

Parameter	Thomas-Fermi Value	Numeric Value	Percentage Difference
Gaussian thickness w_o (ξ)	2.7303	2.7288	0.0541%
$U_{\|\|}$ (ξ^{-4})	9.3868×10^5	9.3580×10^5	0.3076%
Particle Number N	10^5	9.9891×10^4	0.1093%

4.2 Dipoles

Since dipoles appear play an important role in the persistent current decay, we first investigate their properties in the absence of any obstructions.

4.2.1 Homogeneous Systems

The phase of a vortex dipole with vortex separation d, aligned along the y-axis and centred on the x-axis, is given by

$$\begin{aligned}\theta_{\rm dip}(\mathbf{x}) &= \tan^{-1}\left(\frac{y-\frac{d}{2}}{x}\right) - \tan^{-1}\left(\frac{y+\frac{d}{2}}{x}\right) \\ &= -\tan^{-1}\left(\frac{dx}{x^2+y^2-\left(\frac{d}{2}\right)^2}\right),\end{aligned} \tag{4.34}$$

describing a positive (negative) vortex at $y = d/2$ ($y = -d/2$). The phase of a vortex dipole in an arbitrary position and orientation can be found by applying translation and rotation to this expression. We then have derivatives

$$\partial_x\theta_{\rm dip}(\mathbf{x}) = \frac{d\left[r^2\cos 2\theta + (d/2)^2\right]}{(r^2-d^2/4)^2+(dr\cos\theta)^2}, \tag{4.35}$$

$$\partial_y\theta_{\rm dip}(\mathbf{x}) = \frac{d\sin 2\theta}{(r^2-d^2/4)^2+(dr\cos\theta)^2} \tag{4.36}$$

Symmetry requires $\langle P_y\rangle = 0$. Neglecting density gradients near the vortex cores and using equation (4.35), the linear momentum in the x-direction takes the form

$$\langle P_x\rangle = \rho_0\hbar d\int d^2\mathbf{x}\frac{x^2-y^2+(d/2)^2}{[x^2+y^2-(d/2)^2]^2+(dx)^2}. \tag{4.37}$$

Going into cylindrical coordinates, and using the substitution $r = d/2\sqrt{s}$ gives

$$\langle p_x\rangle = \rho_0\hbar d\int_0^{2\pi}d\theta\int_0^\infty\frac{ds}{2s}\frac{s+\cos 2\theta}{1+2s\cos 2\theta+s^2}. \tag{4.38}$$

The integrand is clearly convergent for large s, while for $s\to 0$ there is a divergence in s requiring prior angular integration to obtain a finite result:

$$\langle P_x\rangle = \rho_0\hbar d\frac{\pi}{2}\int_0^\infty ds\frac{s-1+|s-1|}{s^2(s-1)} = \rho_0\hbar d\frac{\pi}{2}\int_1^\infty\frac{ds}{s^2}, \tag{4.39}$$

giving the dipole momentum

$$\langle P_x\rangle = 2\pi\rho_0\hbar d \tag{4.40}$$

where ρ_o is the homogeneous condensate density. We can note from equation (4.39) that, upon angular integration, there is no contribution to the momentum for $r \geq d/2$.

4.2.2 Single Dipole in Tube Trap

In the same vein in which Zhou and Zhai [39] found the angular momentum of a vortex dipole in a harmonic trap, we found the linear momentum of a vortex dipole confined in our tube trap in the Thomas-Fermi approximation.

Consider a dipole where the vector from the anti-vortex to the vortex is $\mathbf{d} = (d_x, d_y)$ present in the tube trap ground state centred a distance D from the x-axis. The separation in the x dimension is irrelevant, so we ignore d_x and relabel $d_y = d$. The quantum mechanical definition of the momentum of the system is

$$\langle P_x \rangle = -i\hbar \int d^2\mathbf{x}\, \Phi^*(x,y) \frac{\partial}{\partial x} \Phi(x,y). \tag{4.41}$$

Employing the Madelung transformation and noting that the condensate density is homogeneous in the x dimension (ignoring the vortex core structure) leads to

$$\langle P_x \rangle = \hbar \int_{-R_y}^{R_y} dy\, \rho(y) \theta(x,y) \Big|_{x=0}^{x=L}. \tag{4.42}$$

Thus we need the change in condensate phase over the system for each value of y. This is only non-zero if the phase jumps in the system, as occurs when passing through a dipole. Hence the change in phase is

$$\theta(x,y)\big|_{x=0}^{x=L} = \begin{cases} 2\pi & \text{if } |y-D| < \frac{d}{2} \\ 0 & \text{otherwise.} \end{cases} \tag{4.43}$$

The momentum is then

$$\langle P_x \rangle = 2\pi\hbar \int_{-d/2+D}^{d/2+D} dy\, \rho(y), \tag{4.44}$$

and using the Thomas-Fermi approximation for the condensate density $\rho(y)$ gives us the final result for our dipole momentum in the tube trap.

$$\langle P_x \rangle = 2\pi\hbar\rho_o d \left(1 - \frac{d^2}{12R_y^2} - \frac{D^2}{R_y^2}\right). \tag{4.45}$$

Inserting $d = 2R_y$ and $D = 0$ into this expression gives the Thomas-Fermi momentum for a dipole separated by the tube width, representing one quanta of winding in the system

$$\langle P_x \rangle = \frac{8}{3}\pi\hbar\rho_o R_y. \tag{4.46}$$

To test this numerically, we create a vortex dipole in a the trap ground state by using phase imprinting, then find the numerical momentum using the quantum mechanical definition. To create a dipole in a particular state we simply add the dipole phase $\theta_{\text{dip}}(\mathbf{x})$ to the phase of the wavefunction. The results of this are shown in Figure 4.3. These show that the analytic expression is very good for a dipole separation up to approximately R_y. The divergence for larger separations is not surprising, as the Thomas-Fermi approximation is less valid at the edges of the condensate, where image vortices become important. Image vortices are somewhat analogous to the image charges that arise in electrostatics for charges near a conductor. The phase signature of a vortex near a boundary is equivalent to that of the

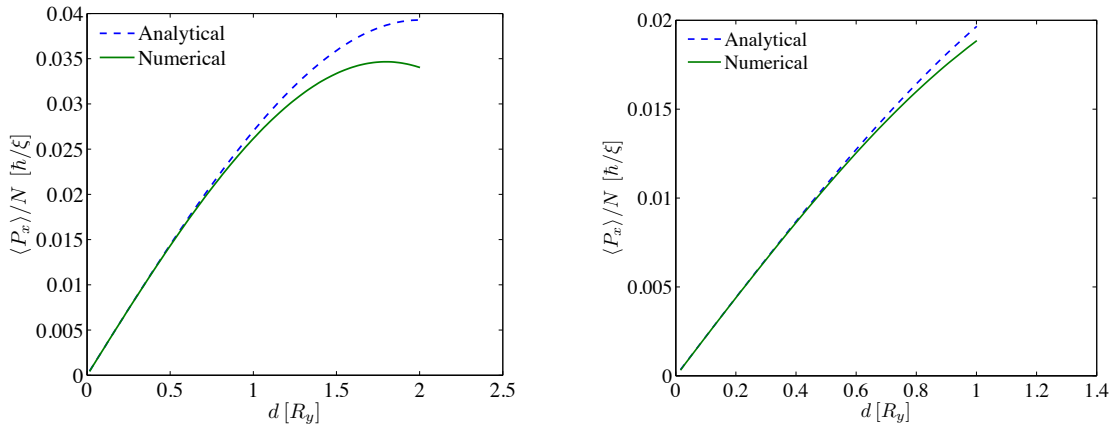

Figure 4.3: Analytic and numerical values of linear momentum carried by a vortex dipole centred on the trap minimum as a function of the dipole separation. The solid green lines are the result of creating a single vortex dipole in the ground state of a condensate in a tube trap and numerically calculating the linear momentum using the quantum mechanical definition. The dashed blue lines are obtained from using the analytical expression (4.45). These are calculated for (a) dipoles centred on the trap minimum ($D = 0$) and (b) dipoles are displaced from the trap minimum by $D = 0.5R_y$.

vortex and its image vortex on the other side of the boundary. The image vortex cancels out the phase that would cause flow normal to the boundary. Thus vortices near the edge of the condensate interact with these image charges, causing significant differences to the motion of vortices in homogeneous systems.

The dipoles in this comparison are ideal, as they are not allowed to evolve with any damping before the calculation of $\langle P_x \rangle$ is made. An ideal dipole consists of just the phase signature of the dipole, with the density being unchanged from the dipole-free system. A true dipole also has a density structure and, in a finite system, image vortices that phase imprinting neglects and is required to eliminate flow normal to the condensate boundary. When evolved in time, an ideal dipole quickly 'relaxes' into a true dipole. Thus to compare our analytic expression with true dipoles, we imprint an ideal dipole into our trap in the presence of a background current, and allow this to evolve with some damping. We use $\gamma = 0.1$ for the damping in this case, so that the polarisation or annihilation proceeds in a smooth fashion. Depending on the initial separation and background current, the dipole will either annihilate or polarise, allowing us to find the momentum for various dipole separations. The background current is described by the winding $n = \pm 5$, and is applied to ensure that the dipole annihilates or polarises as desired. For every time step we find the dipole separation using our vortex detection algorithm, and use this in our analytical expression to find the linear momentum. We also find the numerical momentum at every time step, and compare. The results of this are shown in Figure 4.4. Just like before, the analytical expression is less valid for dipole separations approaching the width of the system.

We also look at the momentum per particle and rate of change of momentum per unit particle for a single dipole polarising in the tube trap. These are shown in Figure 4.5, where the momentum is calculated using the quantum mechanical definition. We can see in the momentum that there is an initial sharp decline, represented in the momentum gradient by

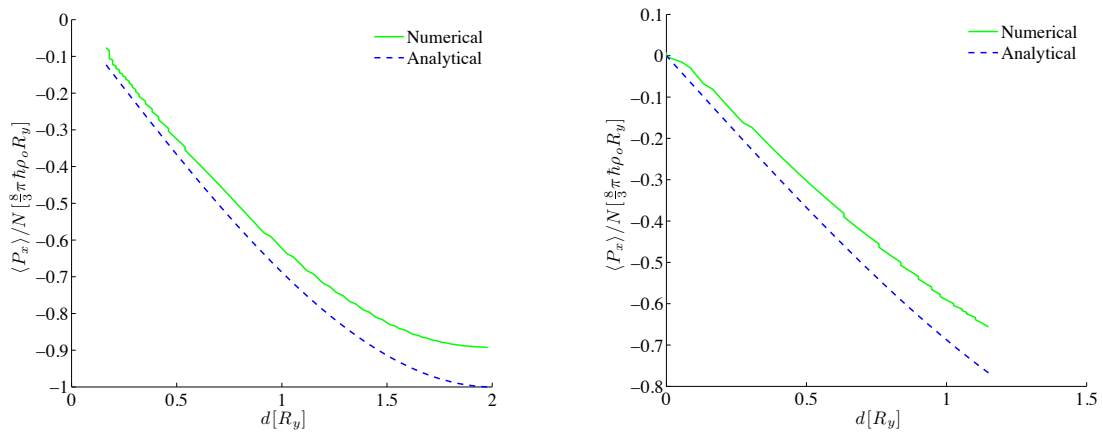

Figure 4.4: Analytic and numerical values of linear momentum carried by a vortex dipole centred on the x-axis as a function of the dipole separation. A single vortex dipole with initial separation $d = 6\xi$ was created in the ground state of a condensate in a tube trap with background winding (a) $n = 5$ or (b) $n = -5$ (b) and evolved in the presence of damping. The dipole then either (a) polarises or (b) annihilates. The solid green line was obtained by numerically calculating the momentum using the quantum mechanical definition at each time step. The dashed blue line was obtained by finding the dipole separation using our vortex detection algorithm at each time step, and then using this with our analytical expression (4.45).

a large negative spike, followed by a steady decline. The sharp jump is due to the initial 'relaxation' of the imprinted ideal dipole to the true dipole.

Critical Separation

When created in the ground state of the tube trap in the absence of any obstruction, and in the presence of dissipation, a vortex dipole will either annihilate or polarise. If the dipole is of the configuration that it carries linear momentum in the *positive* x direction, then polarising increases the linear momentum of the system while annihilating decreases linear momentum. If the dipole is of the configuration that it carries linear momentum in the *negative* x direction, then polarising decreases the linear momentum of the system while annihilating increases linear momentum.

We investigated the critical separation at which a vortex dipole carrying positive linear momentum is in (metastable) equilibrium, that is, it will neither annihilate nor polarise. Below the critical separation, it is energetically favourable for the dipole to annihilate and decrease the linear momentum of system. Above the critical separation, it is energetically favourable for the dipole to polarise and increased the linear momentum of the system. Hence the energy $E(d)$ of a dipole of separation d in the tube trap is unimodal; there is a single maxima at the critical separation. For some initial state, the final state after dipole annihilation will differ from the final state after dipole polarisation by one quanta of winding.

This investigation was performed by applying a winding to the ground state of the trap, then creating a dipole in the system, evolving with some damping and observing whether it polarised or annihilated, and adjusting the initial separation accordingly before repeating

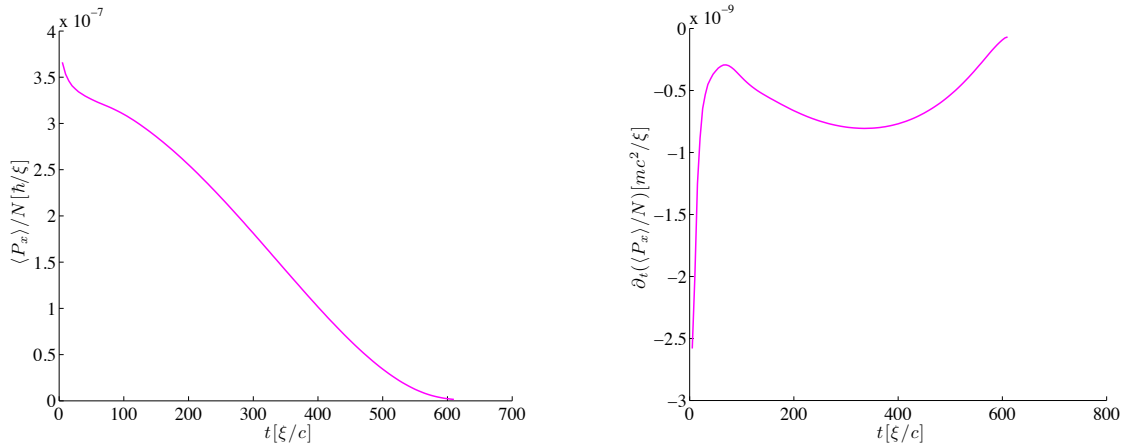

(a) **(b)**

Figure 4.5: Momentum per particle (a) and rate of change of momentum per particle (b) over time during the polarisation of a single dipole. The background current is given by a winding of $n = 5$, and the dipole had an initial separation of $d = 6\xi$. Both the momentum and rate of change of momentum evolve to a final value of zero.

the process. If the dipole polarised, we made the initial separation lower; if the dipole annihilated, we made the initial separation higher. Eventually through this process we found the metastable equilibrium separation representing the critical separation. For a stationary fluid, the critical separation was $0.6336R_y$, slightly more than one quarter of the condensate width. For a fluid with one quanta of winding, the critical separation was $0.9543R_y$, slightly less than half the total condensate width. For a fluid with two quanta of winding the critical separation was $1.1968R_y$.

4.2.3 Dipole Train

To more closely compare to the case of dipole shedding behind an obstacle, we look at the evolution of a dipole train. Similarly to how a dipole was imprinted and evolved with damping to construct Figure 4.4, we imprint a train of ten evenly spaced dipoles of separation $d = 6\xi$ onto the ground state of the tube trap, with a background current described by a winding of $n = 10$ and evolve in the presence of damping. The distance between the dipoles is 16ξ. We then look at the momentum per particle and rate of change of the momentum per particle, both over time. The orientation of the dipoles is such that they polarise, annihilating with vortices in the reservoir and destroying the persistent current.

Notable from this is that there is a small length of time during the polarisation where the rate of change of momentum per particle appears to be linear. This feature can be seen in Figure 4.6b between the times $t \approx 15t_o$ and $t \approx 80t_o$. Although this may be present for the single dipole polarising, it is not clear in Figure 4.5. It may be partially obscured by the 'relaxing' to the true dipole state from the ideal dipole state. It may also be characteristic of the presence of multiple dipoles in the system.

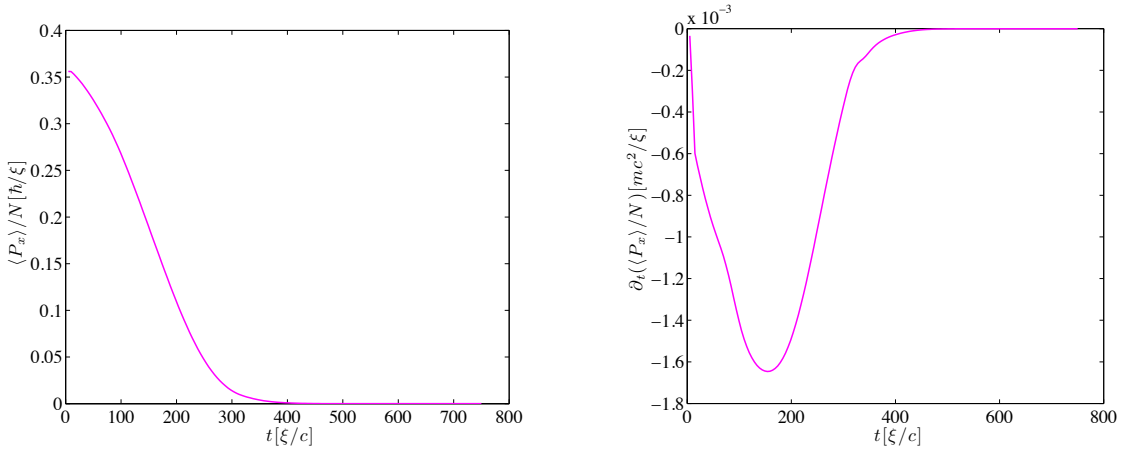

(a) **(b)**

Figure 4.6: Momentum per particle (a) and rate of change of momentum per particle (b) over time for a system during the polarisation of a train of ten dipoles. The background current is given by a winding of $n = 10$, and thus the polarisation of ten dipoles removes all of the linear momentum from the system. The dipoles had an initial separation of $d = 6\xi$. Both the momentum and rate of change of momentum evolve to a final value of zero.

4.3 Obstacles

Here we have stimulated the decay of a persistent current by the introduction of a Gaussian obstacle (see equation (4.24)). This is done by creating a ground state with the obstacle potential already present, then applying the winding to this ground state. This initial state simulates the obstacle and thermal cloud moving in equilibrium with the fluid, before abruptly arresting the obstacle and thermal cloud. We remind the reader that the definition of quantum Reynolds number used here is that suggested by Volovik, given by equation (2.45.

4.3.1 Momentum Decay

The basic phenomenology is that initial states of a given winding will decay if they exceed some critical winding. Furthermore, windings that give an initial velocity less than the Landau critical velocity, that is, the speed of sound ($v_i < v_L = c$), are in many cases unstable. To study the range of possible decay dynamics we choose to simulate the decay for a range of obstacle sizes and initial fluid velocities. The obstacle sizes used are $S_o/\xi = \{4\sqrt{2}, 8\sqrt{2}, 12\sqrt{2}, 16\sqrt{2}, 20\sqrt{2}\}$, while the windings giving the initial fluid velocities are the five lowest that give current decay, and the highest that gives no current decay. Each simulation was performed for a time of $2000t_o$, allowing the systems to reach their new stable state. The highest quantum Reynolds number for these simulations is $Re_s \approx 1.8$, and no significant clustering of vortices is observed.

In Figure 4.7a we show the linear momentum per particle over time for an intermediate initial fluid velocity, for various values of the obstacle width. We can see that, for a large enough obstacle, the momentum decays to a constant non-zero value, indicating the decay of the initial persistent current to a lower winding persistent current. For an obstacle of size $S_o = 4\sqrt{2}\xi$, it is apparent that this initial fluid velocity is below the critical velocity, as there

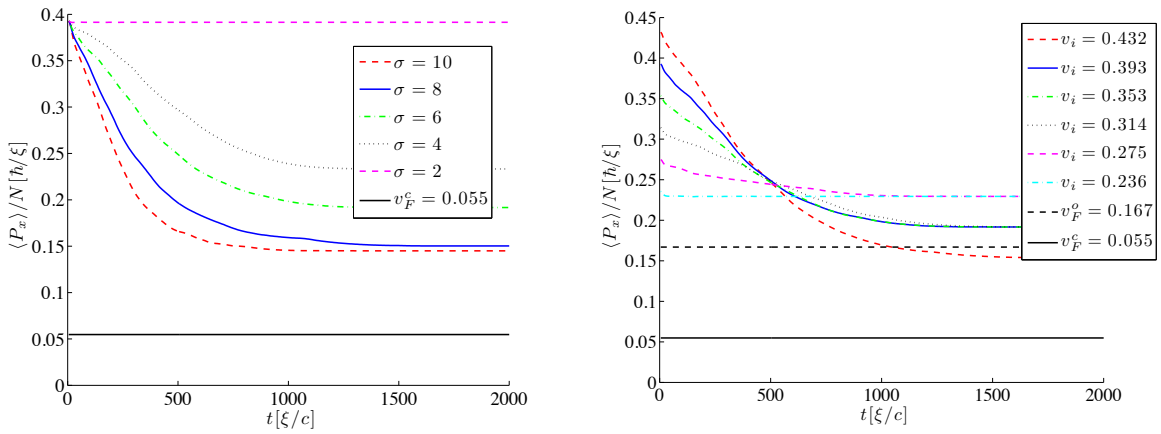

(a) **(b)**

Figure 4.7: (a) Current decay for a winding of $n = 10$, corresponding to an initial velocity of $v_i = 0.3927c$, for various obstacle sizes $S_o = 2\sqrt{2}\sigma$. Also shown is the Feynman critical velocity corresponding to the channel width v_F^c. (b) Current decay for an obstacle of width $S_o = 12\sqrt{2}\xi$, for various initial windings. The critical initial velocity above which excitations occur here is $v_c = 0.1963c$. Also shown is the Feynman critical velocity v_F^o corresponding to the size of this obstacle and the Feynman critical velocity v_F^c corresponding to the width of the channel.

is negligible decrease in the momentum. Looking at Figure 4.7b we observe that the final persistent current velocity appears to be dependent on the initial fluid velocity. We note then, that when persistent current decays, it may decay to a current that is lower than that given by the critical winding for that particular obstacle. In this example, the critical velocity observed is higher than the Feynman critical velocity calculated using the obstacle width (v_F^o), and much greater than the Feynman critical velocity calculated using the channel width (v_F^c). We note that the decay is continuous, indicating that dipoles are playing a central role in the momentum transfer.

We now look slightly more in depth at a particular simulation of current decay. We use the parameters $S_o = 12\sqrt{2}\xi$, the same obstacle size used in Figure 4.7b, and a significantly higher fluid velocity than those shown in Figure 4.7. In this simulation, there appeared to be initial emission of vortex clusters, after which emission became more periodic and the clusters dissociated into individual vortices. This can be seen in Figure 4.8. The quantum Reynolds number in this case is $Re_s \approx 2.1$.

While the decay of momentum is a smooth process, we wish to understand decay in more detail. We expect that, in our dimensionless units, the local velocity and momentum per particle should be very similar (in our dimensionless units) for a system in a stable or metastable state; the only possible difference in that case would be a small shift due to the presence of the obstacle or aperture. However when the system is in a non-equilibrium state we expect the local velocity to vary in space. The change in local velocities may provide more information about the processes behind the current decay.

In Figure 4.9 we compare the local velocity just in front of the obstacle to the momentum per particle of the system, over time. There is a region in time where the local velocity appears to change linearly with time. Looking more closely at this region, we see that the smooth linear region appears to break down at the time where sound waves will have travelled

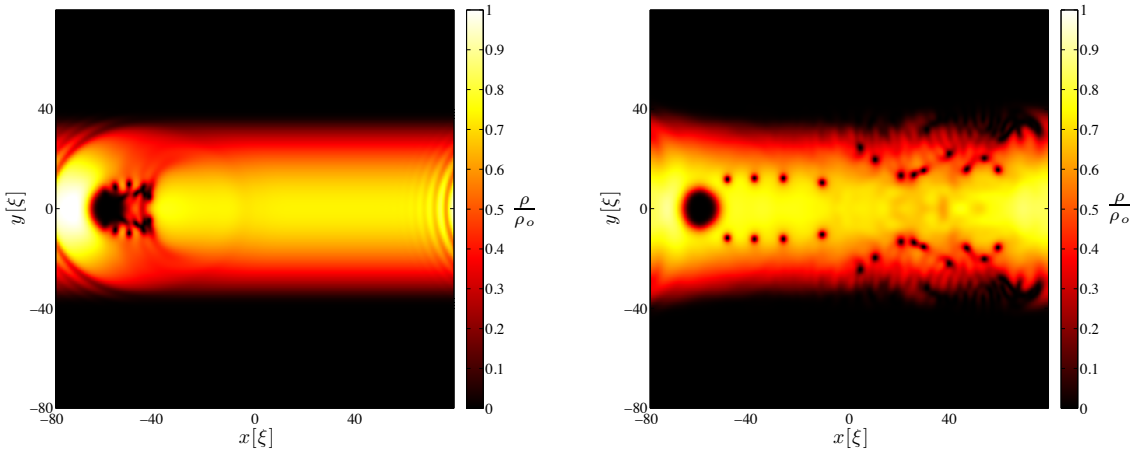

(a) **(b)**

Figure 4.8: Density of the system during time evolution at (a) $t = 40t_o$ and (b) $t = 200t_o$, for a winding of $n = 20$, corresponding to an initial fluid velocity of $v_i = 0.7854c$, in the presence of an obstacle of size $S_o = 12\sqrt{2}\xi$. The density is shown relative to the Thomas-Fermi peak density ρ_o. In (a) we can see what appears to be a large dipole consisting of vortex clusters shedding from behind the obstacle. In (b) the cluster appears to have dissociated into a disordered train configuration, followed by a more ordered train emitted at later times.

the length of the system $t_c = L/c = 160t_o$. This indicates that the breakdown in linearity is most likely due to finite size effects. There is also an initial spike in the local velocity, greater than the initial fluid velocity, which is an early transient caused by the emission of a 'shock wave' from the obstacle. This appears to have subsided after the time at which sound waves will have travelled from the obstacle to the point at which the local velocity is measured $t_p = \Delta x/(c - v_i) \approx 50t_o$, where Δx is the distance from the obstacle edge; the velocity $c - v_i$ is the velocity of sound waves travelling to the left in a fluid travelling to the right at v_i. We note that this initial transient is not present in the momentum decay, which is very smooth at all times. We also show the time for the obstacle to complete one stir of the system $t_v = L/v_i \approx 200t_o$, after which we see a sharp drop in the local velocity and more significant fluctuations.

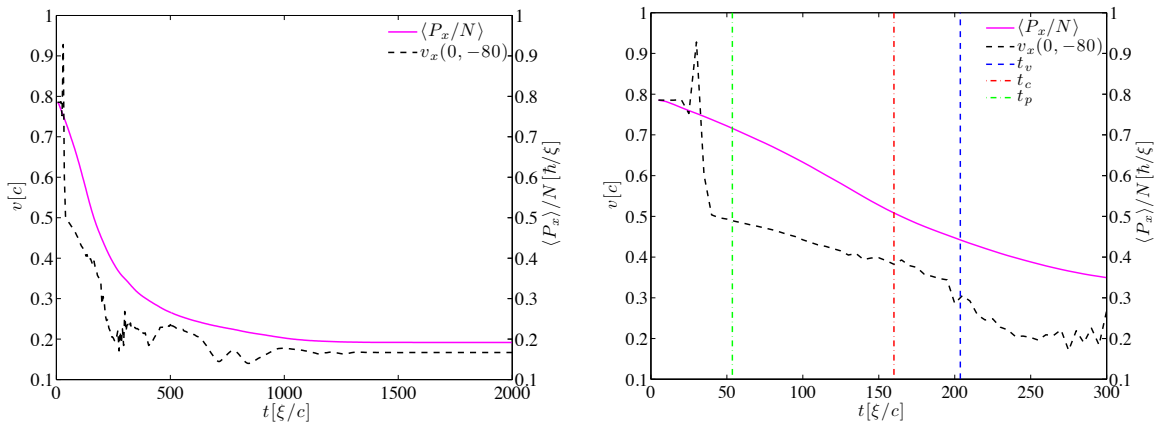

(a) **(b)**

Figure 4.9: Current decay for an obstacle of width $S_o = 12\sqrt{2}\xi$, for an initial winding of $n = 20$. Shown in (a) is the linear momentum per particle and local velocity in front of the obstacle, over time. In (b) we present the same data, but zoomed into the region $t \in [0, 300t_o]$. Also shown are the time at which sound waves will have travelled the length of the system ($t_c = 160t_o$), the time at which the obstacle completes one stir of the system ($t_v \approx 200t_o$), and the time at which sound waves emitted from the obstacle will reach the point at which the local velocity is measured ($t_p \approx 50t_o$).

4.3.2 Force

For this subsection, we continue to look at the simulation discussed at the end of the previous section, focusing on the forces acting on the persistent current as it decays.
We investigate the force per particle due to the obstacle over time during the current decay, and compare to the rate of change of momentum per particle. The force is given by the expression

$$\begin{aligned}\mathbf{F} &= -\int d^2\mathbf{x}\Phi^*(x,y)\nabla V_{||}(x,y)\Phi(x,y) \\ &= \int d^2\mathbf{x}V_{||}(x,y)\nabla\rho(x,y)\end{aligned} \tag{4.47}$$

The force in the y dimension F_x is very small, and so we only look at F_x. This is presented in Figure 4.10a, along with the rate of change of momentum per particle for the polarisation of a dipole train of ten dipoles of initial separation $d = 6\xi$, spaced evenly along the domain in the presence of a background winding $n = 10$. We compare this to Figure 4.10b, the force and rate of change of momentum for the same parameters with the exception of the initial fluid velocity, which we change to the highest initial velocity for an obstacle of width $S_o = 12\sqrt{2}\xi$ which did not result in dipole emission. The notable difference between these two is that, without emission the force and momentum gradient are equal, whereas when emission is present the force and momentum gradient are not the same. There is an initial transient in Figure 4.10b due to the shedding of sound waves as the fluid adjusts to the motion of the obstacle, but this is small compared to the values in Figure 4.10a. Comparing with the dipole train momentum gradient, it appears that, qualitatively at least, the difference between the force and momentum gradient is caused by the damping induced polarisation of dipoles. This is clearly shown for $t \lesssim 200t_o$, where the polarisation of the dipole train imparts a linear 'force' on the persistent current.

In the absence of damping, a Gross-Pitaevskii model predicts that a quantum vortex in a quasi-two-dimensional condensate will not spontaneously decay [40]. Thus we compare the simulation in the presence of damping to that without. The simulation with no damping ($\gamma = 0$) is shown in Figure 4.11, along with the same data for an initial current described by the winding $n = 7$, the lowest for which decay occurs. In these cases, the force on the obstacle per particle and rate of change of momentum per particle are identical, and thus we can safely say that the difference between these is due to the damping on the system inducing the polarisation of dipoles. Even in the presence of damping, there is no difference between force and momentum gradient for simulations where vortex emission is absent.

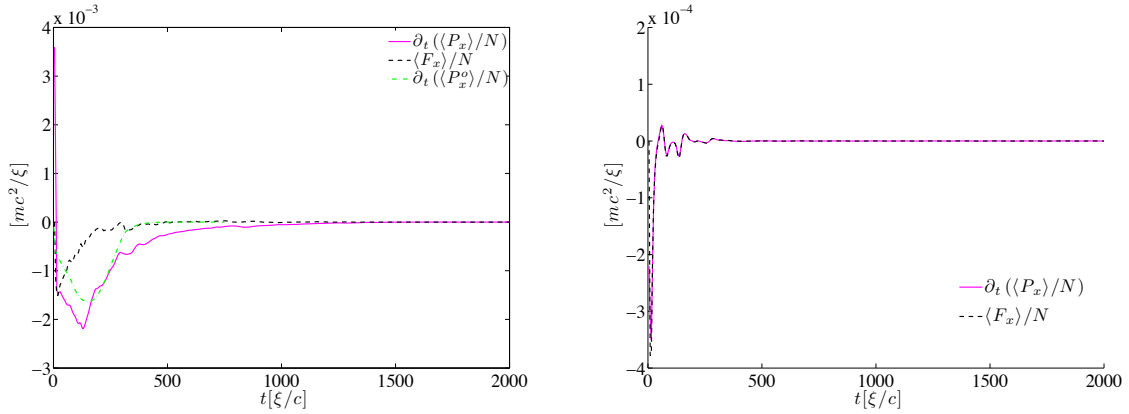

(a) **(b)**

Figure 4.10: (a) Current decay for an obstacle of width $S_o = 12\sqrt{2}\xi$, for a winding of $n = 20$. Shown is the force per particle and rate of change of momentum per particle over time. Also shown is the rate of change of momentum per particle over time for the polarisation of the dipole train, as shown in Figure 4.6b. The momentum for the dipole train is denoted by P_x^o. (b) The same data with the exception that the winding is $n = 6$, which is the highest winding for which no vortex emission occurs for this obstacle size.

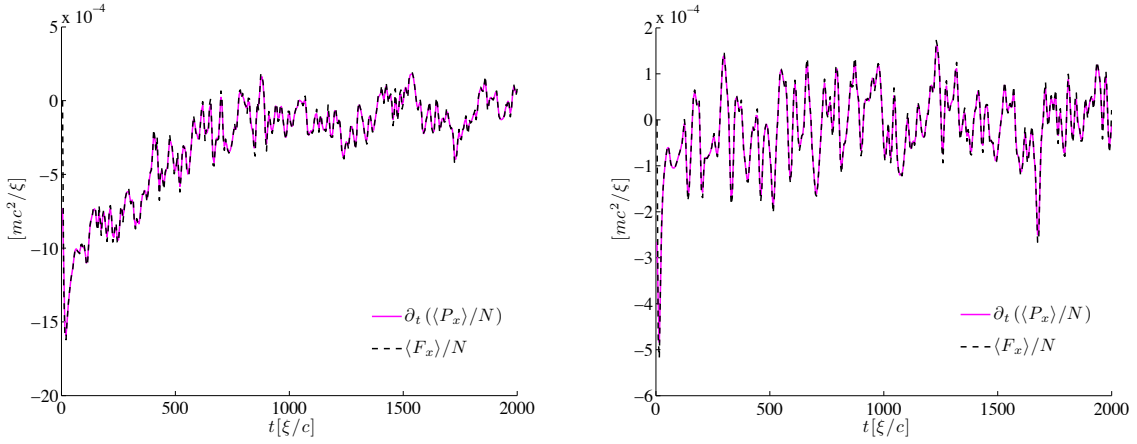

(a) **(b)**

Figure 4.11: Current decay for an obstacle of width $S_o = 12\sqrt{2}\xi$ in the absence of damping. Shown is the force per particle and rate of change of momentum per particle over time. In (a) the initial current is given by the winding $n = 20$, while in (b) the initial current is given by the winding $n = 7$, the lowest for which dipole emission is observed.

4.4 Apertures

As alluded to in section (2.2.4), an obstruction that acts as a direct contrast to an obstacle is the aperture. In this case, vortex anti-dipoles nucleate from the lobes of the aperture and undergo motion to the centre of the tube and annihilate.

Here we have stimulated the decay of a persistent current by the introduction of an aperture potential (see equation (4.25)). This is done by creating a ground state with the aperture potential already present, then applying the winding to this ground state. This simulates the aperture and thermal cloud moving in equilibrium with the fluid, before abruptly arresting the aperture and thermal cloud.

4.4.1 Momentum Decay

We performed simulations for the aperture sizes $S_a/\xi = \{5,\ 10,\ 15,\ 20,\ 25\}$. To explore the basic phenomena we simulated the dynamics for a range of initial fluid velocities for each obstacle. As for the obstacle, the windings giving the initial fluid velocities are the five lowest that give current decay, and the highest that gives no current decay. Each simulation was performed for a time of $2000t_o$, to ensure that a steady state was reached. In these simulations no clustering of vortices is observed.

In Figure 4.12a we show the linear momentum per particle over time for an initial fluid velocity of $v_i = 0.2356c$, for a range of aperture sizes. Included is the limiting case as the aperture shrinks into an impenetrable barrier, $S_a = 0$, which shows a fast decay to the stationary ground state. We can see that, apart from the limiting barrier case, the momentum decays to a constant non-zero value, indicating the decay of the initial persistent current to a lower winding persistent current. This initial velocity is greater than the observed critical velocity for each of the aperture sizes considered. For each aperture, the current decays

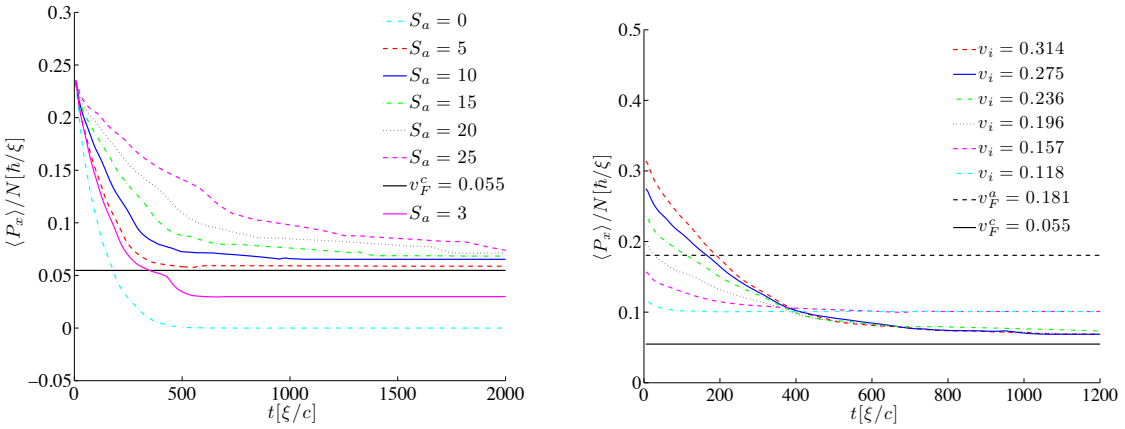

(a) **(b)**

Figure 4.12: (a) Current decay for a winding of $n = 6$, corresponding to an initial velocity of $v_i = 0.2356c$, for various aperture sizes S_a. Also shown is the Feynman critical velocity found using the channel width v_F^c. (b) Current decay for an aperture of width $S_o = 15\xi$, for various initial windings. Also shown is Feynman critical velocity found using the channel width v_F^c and the aperture width v_F^a. The critical initial velocity above which excitations are observed here is $v_c = 0.1178c$, corresponding to a winding of $n = 3$.

to a similar value, but smaller apertures cause the decay to proceed more rapidly. Figure 4.12b shows that the current may decay to a value lower than that given by the observed critical velocity. However, in simulations for a smaller aperture size, all five of the windings considered resulted in decay to the same current value. This value also corresponded to the highest winding that did not induce current decay. For narrow apertures, the observed critical velocity was consistent with the Feynman critical velocity calculated using the channel width. The decay is continuous, indicating that dipoles are playing a role in the momentum transfer. There is a large drop in the final current velocity between the aperture sizes $S_a = 0$ and $S_a = 5$. Thus we also show in Figure 4.12b the the momentum decay for the aperture width S_a. This shows that, as the aperture size gets close to the healing length, the physics of the decay undergoes a transition. We note that the data for Figures 4.12 and 4.7, and similar plots not included here, formed the vast majority of the total data obtained for this work.

We now look slightly more in depth at a particular simulation of current decay. We use the parameters $S_a = 15\xi$, the same aperture size used in Figure 4.12b, and a significantly higher fluid velocity than those used in Figure 4.12. In this simulation, there appears to be some vortex clustering during the early stages of emission, before emission becomes more periodic. We also observe vortices circulating in the regions behind the aperture lobes.

In Figure 4.14 we compare the local velocity just in front of the centre of the aperture to the momentum per particle of the system, over time. There is a region early in time where the local velocity appears to change linearly in time. This appears to break down and become more erratic at approximately the time it takes for sound waves to travel the length of the system $t_c = L/c = 160t_o$. There is also an initial transient that appears to have subsided by the time that sound waves have travelled from the aperture center to the point at which

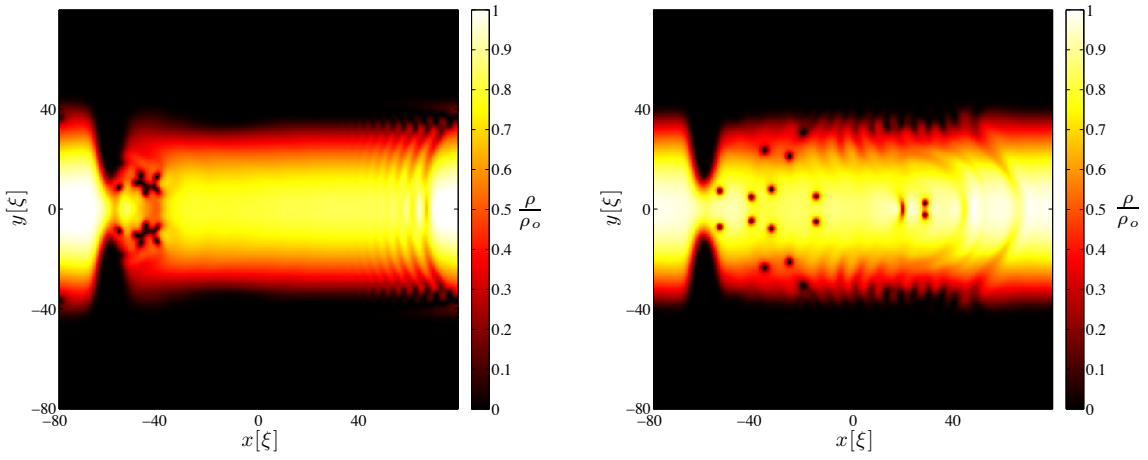

(a) **(b)**

Figure 4.13: Density of the system during time evolution at (a) $t = 60t_o$ and (b) $t = 200t_o$, for a winding of $n = 15$, corresponding to an initial fluid velocity of $v_i = 0.5890c$, in the presence of an aperture of size $S_o = 15\xi$, where ρ_o is the maximum condensate density. In (a) we can see what appears to a large dipole consisting of vortex clusters shedding from behind the aperture. In (b) the cluster has have dissociated, with some dipoles moving along the tube and annihilating, while some of the vortices have moved to circulate in the area behind the aperture lobes. We also observe periodic dipole emission at this stage.

the local velocity was measured, $t_p = \Delta x/(c - v_i) \approx 50t_o$, where Δx is the distance from the aperture. We note that the local velocity spikes at several points after this time. This is most likely due to the velocity signature of passing vortices, as some dipoles had travelled more than the system length by the time they annihilated. This is very much a finite size effect. We have also marked the time at which excitations travelling at the initial velocity will have travelled the entire system $t_v = L/v_i \approx 270t_o$, after which more fluctuations occur, including those due to the velocity signature of passing vortices.

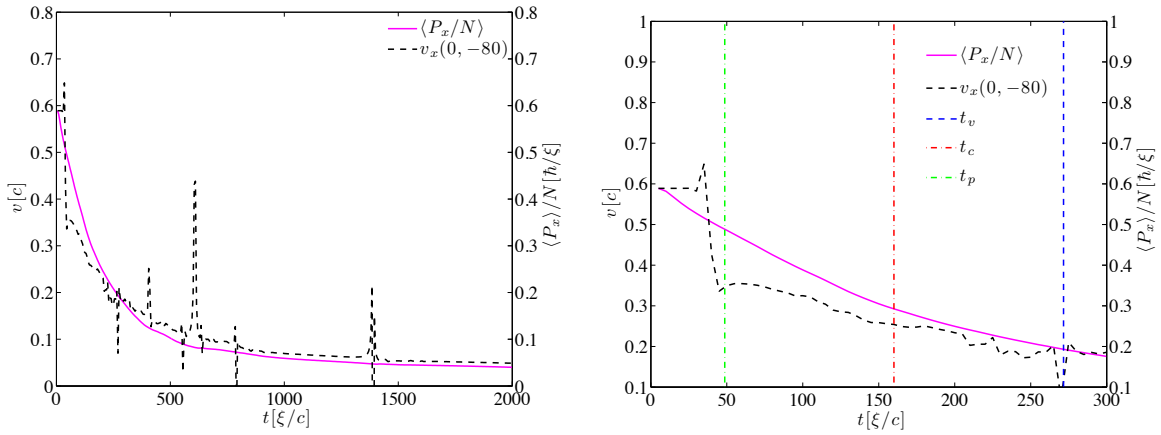

(a) **(b)**

Figure 4.14: Current decay for an aperture of width $S_a = 15\xi$, for an initial winding of $n = 15$. Shown is the linear momentum per particle and local velocity in front of the aperture centre, over time. Also marked in (a) are the time at which sound waves will have travelled the length of the system (t_c), and the time at which vortices travelling at the initial velocity will have travelled the length of the system (t_v). In (b) we present the same data, but zoomed into the region $t \in [0, 200t_o]$. Also shown is the time for sound waves to travel from the aperture centre to the point where the local velocity is measured (t_p).

4.4.2 Force

For this subsection, we continue to look at the simulation discussed at the end of the previous section, focusing on the forces acting on the persistent current as it decays.

We investigate the force per particle due to the aperture over time during current decay, and compare to the rate of change of momentum per particle. The force is given by equation (4.47). This data is presented in Figure 4.15a. We compare this to Figure 4.15b, the force and rate of change of momentum per particle for the same parameters with the exception of the initial fluid velocity, which we change to the highest initial velocity for an aperture of width $S_a = 15\xi$ which did not result in dipole emission. For the simulation with no emission, the force and momentum gradient are equal, whereas the simulation with emission shows that the magnitude of the force is generally less than that of the momentum gradient. It appears that this feature is caused by the damping-induced annihilation of dipoles.

We also compare the simulation in the presence of damping to that without. The simulation without damping ($\gamma = 0$)is shown in Figure 4.16, for initial velocities described by the windings $n = 15$ and also $n = 3$, the highest for which emission is not observed. The figures show that if no damping is present, the force and rate of change of momentum per particle are identical, and thus the difference observed in the simulations with non-zero damping is due to the damping inducing dipole annihilation.

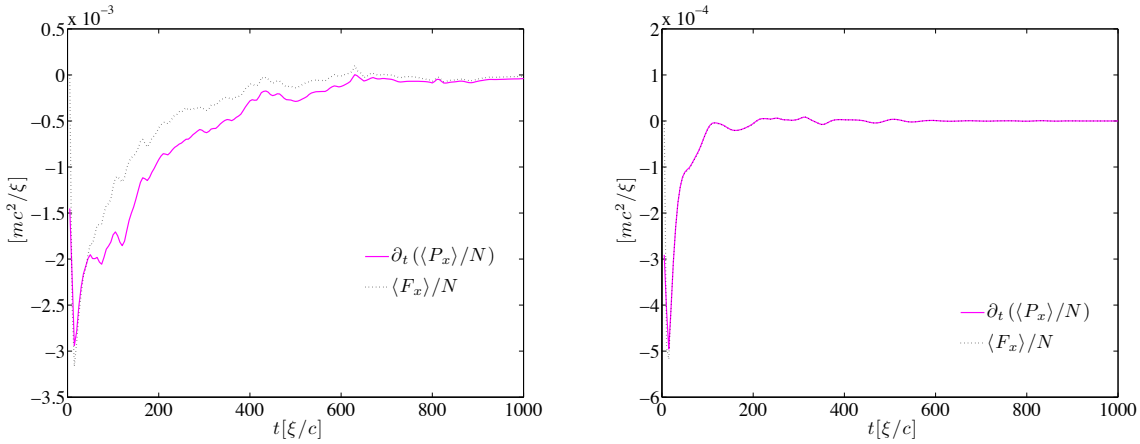

(a) **(b)**

Figure 4.15: (a) Current decay for an aperture of width $S_a = 15\xi$, for a winding of $n = 15$, corresponding to an initial velocity of $v_i = 0.5890c$. Shown is the force per particle and rate of change of momentum per particle over time.(b) The same data with the exception that the winding is $n = 3$, corresponding to an initial velocity of $v_i = 0.1178c$, the highest for which no vortex emission occurs for this aperture size.

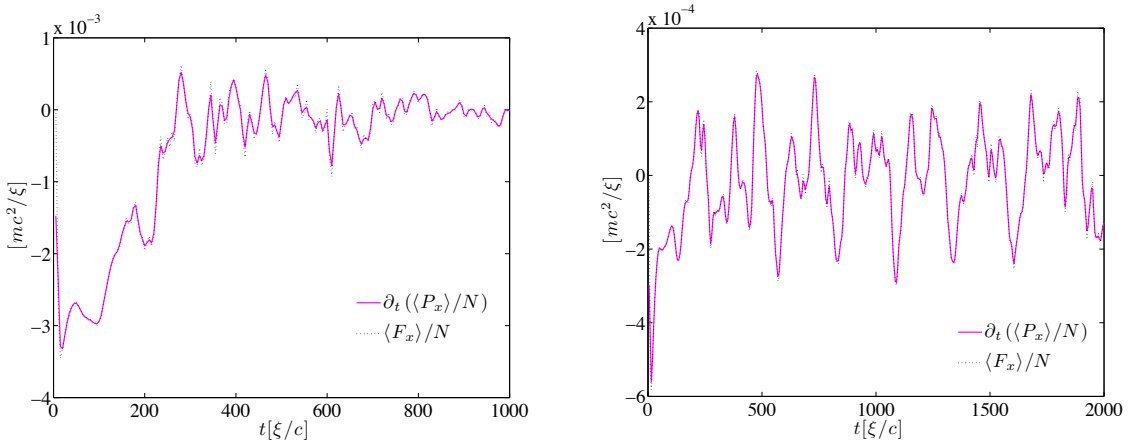

(a) **(b)**

Figure 4.16: Current decay for an aperture of width $S_a = 15\xi$ in the absence of damping. Shown is the force per particle and rate of change of momentum per particle over time. In (a) the initial current is given by the winding $n = 15$, corresponding to an initial fluid velocity of $v_i = 0.5890c$. In (b) the initial current is given by the winding $n = 3$, corresponding to an initial fluid velocity of $v_i = 0.1178c$ the highest for which dipole emission is not observed.

4.5 Comparisons

In this section, we summarise the similarities and differences in current decay when induced with an obstacle or aperture.

The aperture potentials, in general, caused evolution to a stable state to be faster than for obstacle potentials. The dipoles appeared to annihilate much quicker than polarise. The results of finding the critical separation seemed to imply that annihilation of dipoles was somehow more favoured than polarisation, which may be the cause of this more rapid decay.

The dipoles emitted from the aperture move into the condensate center, where the fluid is approaching homogeneity. The dipoles emitted from the obstacle move out to the condensate edge, where the inhomogeneity of the fluid becomes important, as does interaction with image vortices. This may partially explain why aperture-induced decay is much faster than obstacle-induced decay, as the vortices near the condensate edge are somewhat repelled by image charges of the same sign.

The steps between the aperture sizes ($\Delta S_o = 5\xi$) and the steps between the obstacle sizes ($\Delta S_o = 5.56\xi$) were similar, yet changing the obstacle size had a more significant affect on the critical velocity than changing the aperture size.

Both obstacle and aperture decay in the presence of damping had the magnitude of the rate of change of momentum per particle greater than the force on the obstacle/aperture per particle, an effect consistent with dipole polarisation or annihilation induced by the dissipation.

Chapter 5

Conclusions

5.1 Summary

In this study we have investigated the decay of persistent currents in two-dimensional Bose-Einstein condensates, using a phenomenologically damped Gross-Pitaevskii model with modifications from the hybrid Lagrangian variational method.

We first developed the hybrid Lagrangian variational method as a modification to Gross-Pitaevskii theory to describe less anisotropic systems than just the two-dimensional Gross-Pitaevskii equation can accurately describe. We test the ground states found from this by comparing to Thomas-Fermi predictions, and find good agreement. We also find that the hybrid Lagrangian variational method tends toward the original Gross-Pitaevskii model for high anisotropies.

We used an overdamped system to test an analytical expression for the linear momentum of a vortex dipole in a linear harmonic trap that we derived. We found that the approximations used in finding the expression worked very well for small dipole separations, becoming less valid for separations close to the system size, but still quite accurate. We also looked into critical separations for dipoles in the presence of winding in the system.

We investigated current decay for a range of initial current velocities, aperture sizes, and obstacle sizes. Our investigation found that the critical velocity for decay to occur is dependent on the obstacle or aperture size. However the results of [26] suggest that, in the homogeneous system, the critical velocity is not dependent on obstacle size or shape. We also found that initial current velocities much higher than the critical velocity can induce current decay that results in a stable current less than the critical velocity. Thus we conclude from this that the final velocity in current decay is dependent on the initial velocity. We also found that aperture induced current decay approaches a fluid velocity consistent with the Feynman critical velocity calculated for the channel width. except for aperture widths approaching the healing length.

We looked more in depth at two particular cases of current decay, one for an obstacle and one for an aperture, from a higher initial velocity. The velocities chosen for this showed vortex clustering in the early time evolution. The local velocity directly in front of the obstacle or

aperture decayed in a fashion similar to the global momentum per particle. However a linear region of decay was observed after an initial transient, but before sound waves had travelled the length of the system. After this time the local velocity decay became more erratic.

We looked at the force per particle and rate of change of momentum per particle for these current decays. We found that in the presence of damping, the force on the obstruction is less than the rate of change of momentum whenever vortex emission is observed. This lead us to conclude that the damping induced polarisation/annihilation of vortices is an important mechanism behind current decay in the systems we simulated.

Our comparison of aperture and obstacle stimulated decays turned up some interesting questions. In particular, it is unclear what length scales are of interest in the aperture decay, and whether the aperture and obstacle are truly distinct.

Future Work

During this work, questions were raised about the dependence of the critical velocity on object and aperture sizes. In particular, the validity of Feynman's expression came under some scrutiny; this is an area we would like to investigate. We would also like to investigate critical velocities in homogeneous systems to determine if and how they depend on the length scales of obstructions. We would also like to extend the persistent current investigation in this work to a true toroidal geometry.

Bibliography

[1] M. Tsubota. Quantum turbulence: from superfluid helium to atomic Bose-Einstein condensates. *Journal of Physics Condensed Matter*, 21(16):164207, April 2009.

[2] Pijush K. Kundu, Ira M. Cohen, David R. Downling. *Fluid Mechanics*. Academic Press, 2012.

[3] M. T. Reeves, T. P. Billam, B. P. Anderson, and A. S. Bradley. Inverse Energy Cascade in Forced Two-Dimensional Quantum Turbulence. *Physical Review Letters*, 110(10):104501, March 2013.

[4] C. Ryu, M. F. Andersen, P. Cladé, V. Natarajan, K. Helmerson, and W. D. Phillips. Observation of Persistent Flow of a Bose-Einstein Condensate in a Toroidal Trap. *Physical Review Letters*, 99(26):260401, December 2007.

[5] B. V. Rollin and F. Simon. On the "film" phenomenon of liquid helium II. *Physica*, 6:219–230, February 1939.

[6] G. J. C. Bots and C. J. Gorter. Fountain Effect in Helium II below 1° K. *Phys. Rev.*, 90:1117–1118, Jun 1953.

[7] M. H. Anderson, J. R. Ensher, M. R. Matthews, C. E. Wieman, and E. A. Cornell. Observation of Bose-Einstein Condensation in a Dilute Atomic Vapor. *Science*, 269(5221):198–201, 1995.

[8] Franco Dalfovo, Stefano Giorgini, Lev P. Pitaevskii, and Sandro Stringari. Theory of Bose-Einstein condensation in trapped gases. *Rev. Mod. Phys.*, 71:463–512, Apr 1999.

[9] T. W. Neely, E. C. Samson, A. S. Bradley, M. J. Davis, and B. P. Anderson. Observation of Vortex Dipoles in an Oblate Bose-Einstein Condensate. *Phys. Rev. Lett.*, 104:160401, Apr 2010.

[10] M. Edwards, M. Krygier, H. Seddiqi, B. Benton, and C. W. Clark. Approximate mean-field equations of motion for quasi-two-dimensional Bose-Einstein-condensate systems. *Phys. Rev. E*, 86(5):056710, November 2012.

[11] S. J. Rooney, P. B. Blakie, B. P. Anderson, and A. S. Bradley. Suppression of Kelvon-induced decay of quantized vortices in oblate Bose-Einstein condensates. *Phys. Rev. A*, 84:023637, Aug 2011.

[12] Allan Griffin, Tetsuro Nikuni and Eugene Zaremba. *Bose-Condensed Gases at Finite Temperatures*. Cambridge University Press, 2009.

[13] A. L. Fetter and A. A. Svidzinsky. TOPICAL REVIEW: Vortices in a trapped dilute Bose-Einstein condensate. *Journal of Physics Condensed Matter*, 13:135, March 2001.

[14] V.A. Mironov, A.I. Smirnov, and L.A. Smirnov. Structure of Vortex Shedding Past Potential Barriers Moving in a Bose-Einstein Condensate. *Journal of Experimental and Theoretical Physics*, 110(5):877–889, 2010.

[15] K. Sasaki, N. Suzuki, and H. Saito. Bénard-von Kármán Vortex Street in a Bose-Einstein Condensate. *Physical Review Letters*, 104(15):150404, April 2010.

[16] A. S. Bradley and B. P. Anderson. Energy Spectra of Vortex Distributions in Two-Dimensional Quantum Turbulence. *Physical Review X*, 2(4):041001, October 2012.

[17] S. Choi, S. A. Morgan, and K. Burnett. Phenomenological damping in trapped atomic Bose-Einstein condensates. *Phys. Rev. A*, 57:4057–4060, May 1998.

[18] G. E. Volovik. Classical and Quantum Regimes of Superfluid Turbulence. *Soviet Journal of Experimental and Theoretical Physics Letters*, 78:533–537, November 2003.

[19] D. S. Rokhsar. Vortex Stability and Persistent Currents in Trapped Bose Gases. *Phys. Rev. Lett.*, 79:2164–2167, Sep 1997.

[20] Juha Javanainen, Sun Mok Paik, and Sung Mi Yoo. Persistent currents in a toroidal trap. *Phys. Rev. A*, 58:580–583, Jul 1998.

[21] Anthony E. Siegman. *LASERS*. University Science Books, 1986.

[22] M. Modugno, C. Tozzo, and F. Dalfovo. Detecting phonons and persistent currents in toroidal Bose-Einstein condensates by means of pattern formation. *Phys. Rev. A*, 74(6):061601, December 2006.

[23] Ögren, M. and Kavoulakis, G.M. Stability of Persistent Currents in a Bose-Einstein Condensate Confined in a Toroidal Trap. *Journal of Low Temperature Physics*, 154(1-2):30–40, 2009.

[24] S. Franke-Arnold, J. Leach, M. J. Padgett, V. E. Lembessis, D. Ellinas, A. J. Wright, J. M. Girkin, P. Ohberg, and A. S. Arnold. Optical ferris wheel for ultracold atoms. *Optics Express*, 15:8619–8625, July 2007.

[25] T. Winiecki, J. F. McCann, and C. S. Adams. Pressure Drag in Linear and Nonlinear Quantum Fluids. *Physical Review Letters*, 82:5186–5189, June 1999.

[26] T. Frisch, Y. Pomeau, and S. Rica. Transition to dissipation in a model of superflow. *Phys. Rev. Lett.*, 69:1644–1647, Sep 1992.

[27] L. Landau. Theory of the Superfluidity of Helium II. *Phys. Rev.*, 60:356–358, Aug 1941.

[28] Juha Javanainen and Yi Zheng. Perturbing a persistent current with an external potential. *Phys. Rev. A*, 63:063610, May 2001.

[29] R.P. Feynman. *Statistical mechanics: a set of lectures*. Frontiers in physics. W. A. Benjamin, 1972.

[30] A. Ramanathan, K. C. Wright, S. R. Muniz, M. Zelan, W. T. Hill, III, C. J. Lobb, K. Helmerson, W. D. Phillips, and G. K. Campbell. Superflow in a Toroidal Bose-Einstein Condensate: An Atom Circuit with a Tunable Weak Link. *Physical Review Letters*, 106(13):130401, April 2011.

[31] F. Piazza, L. A. Collins, and A. Smerzi. Critical velocity for a toroidal Bose-Einstein condensate flowing through a barrier. *Journal of Physics B Atomic Molecular Physics*, 46(9):095302, May 2013.

[32] A. C. Mathey, C. W. Clark, and L. Mathey. Decay of a superfluid current of ultra-cold atoms in a toroidal trap. *ArXiv e-prints*, July 2012.

[33] K. B. Davis, M. O. Mewes, M. R. Andrews, N. J. van Druten, D. S. Durfee, D. M. Kurn, and W. Ketterle. Bose-Einstein Condensation in a Gas of Sodium Atoms. *Phys. Rev. Lett.*, 75:3969–3973, Nov 1995.

[34] C. C. Bradley, C. A. Sackett, J. J. Tollett, and R. G. Hulet. Evidence of Bose-Einstein Condensation in an Atomic Gas with Attractive Interactions. *Phys. Rev. Lett.*, 75:1687–1690, Aug 1995.

[35] Matthew T. Reeves. Two-Dimensional Quantum Turbulence in Stirred Bose-Einstein Condensates, 2011.

[36] R. Onofrio, C. Raman, J. M. Vogels, J. R. Abo-Shaeer, A. P. Chikkatur, and W. Ketterle. Observation of Superfluid Flow in a Bose-Einstein Condensed Gas. *Phys. Rev. Lett.*, 85:2228–2231, Sep 2000.

[37] K. Henderson, C. Ryu, C. MacCormick, and M. G. Boshier. Experimental demonstration of painting arbitrary and dynamic potentials for Bose-Einstein condensates. *New Journal of Physics*, 11(4):043030, April 2009.

[38] B. M. Caradoc-Davies. *Vortex Dynamics in Bose-Einstein Condensates*. PhD thesis, University of Otago, Dunedin, New Zealand, 2000.

[39] Q. Zhou and H. Zhai. Vortex dipole in a trapped atomic Bose-Einstein condensate. *Phys. Rev. A*, 70(4):043619, October 2004.

[40] S. J. Rooney, A. S. Bradley, and P. B. Blakie. Decay of a quantum vortex: Test of nonequilibrium theories for warm Bose-Einstein condensates. *Phys. Rev. A*, 81:023630, Feb 2010.